Behavior of Colloids with Anisotropic Diffusivities

by

Nathan Arasmus Marine

A Dissertation Presented in Partial Fulfillment
of the Requirements for the Degree
Doctor of Philosophy

Approved July 2013 by the
Graduate Supervisory Committee:

Jonathan D. Posner, Chair
Ronald Adrian
David Frakes
Patrick Phelan
Veronica Santos

ARIZONA STATE UNIVERSITY

August 2013

ABSTRACT

Locomotion of microorganisms is commonly observed in nature and some aspects of their motion can be replicated by synthetic motors. Synthetic motors rely on a variety of propulsion mechanisms including auto-diffusiophoresis, auto-electrophoresis, and bubble generation. Regardless of the source of the locomotion, the motion of any motor can be characterized by the translational and rotational velocity and effective diffusivity. In a uniform environment the long-time motion of a motor can be fully characterized by the effective diffusivity. In this work it is shown that when motors possess both translational and rotational velocity the motor transitions from a short-time diffusivity to a long-time diffusivity at a time of π/ω. The short-time diffusivities are two to three orders of magnitude larger than the diffusivity of a Brownian sphere of the same size, increase linearly with concentration, and scale as $v^2/2\omega$. The measured long-time diffusivities are five times lower than the short-time diffusivities, scale as $v^2/\{2Dr\,[1 + (\omega/Dr\ )^2]\}$, and exhibit a maximum as a function of concentration. The variation of a colloid's velocity and effective diffusivity to its local environment (e.g. fuel concentration) suggests that the motors can accumulate in a bounded system, analogous to biological chemokinesis. Chemokinesis of organisms is the non-uniform equilibrium concentration that arises from a bounded random walk of swimming organisms in a chemical concentration gradient. In non-swimming organisms we term this response *diffusiokinesis*. We show that particles that migrate only by Brownian thermal motion are capable of achieving non-uniform pseudo equilibrium distribution in a diffusivity gradient. The concentration is a result of a bounded random-walk process where at any given time a larger percentage of particles can be found in the regions of low diffusivity

than in regions of high diffusivity. Individual particles are not trapped in any given region but at equilibrium the net flux between regions is zero. For Brownian particles the gradient in diffusivity is achieved by creating a viscosity gradient in a microfluidic device. The distribution of the particles is described by the Fokker-Planck equation for variable diffusivity. The strength of the probe concentration gradient is proportional to the strength of the diffusivity gradient and inversely proportional to the mean probe diffusivity in the channel in accordance with the no flux condition at steady state. This suggests that Brownian colloids, natural or synthetic, will concentrate in a bounded system in response to a gradient in diffusivity and that the magnitude of the response is proportional to the magnitude of the gradient in diffusivity divided by the mean diffusivity in the channel.

DEDICATION

To my family.

ACKNOWLEDGEMENTS

I would like to thank my committee comprised of Dr. Ronald Adrian, Dr. David Frakes, Dr. Patrick Phelan, and Dr. Veronica Santos for all of their help and guidance from my comprehensive exams through my dissertation defense. I especially thank my advisor and committee chair Dr. Jonathan D. Posner for his guidance and support throughout my graduate studies at Arizona State University.

I also thank my colleagues in the Posner Research Group. Specifically I thank: Philip Wheat for teaching me how to use the tools in the clean room and nanomotors, Steven Klein for teaching me how to use how to use the TE 2000, and Jeff Moran for always being ready to discuss any difficult analysis. I also want to specifically acknowledge Babak Moghadam, Guru Navaneetham, Kamil Salloum, Juan Tibaquira, Carlos Perez, and Wen-Che Hou for thoughtful discussions and input throughout my studies. I especially thank Charlie Corredor and Jeff Moran for their tremendous efforts to help keep me supplied during my solo act at ASU. I would like to thank the staff in CSSER and CSSS for their instruction and for the use of their facilities throughout my research.

I am extremely grateful to Dr. Kyle Squires for funding me during my final two years and allowing me to opportunity to try my hand as a lecturer. Without his help the completion of my studies would not have been possible.

I am eternally grateful to my family for their help and support. To my mom, Cheryle, my brother, Zachary, and my little sister, Sierra for the Sundays filled with fun, games, and home cooked food. To my dad, Jeff, and mom, Sharon, for their unwavering love and support and for teaching me the importance of working hard in school. To my

sister Naomi for being a lifelong companion and for our recent summers backpacking. Lastly, I would like to thank my grandparents James and Maxine Marine for always being ready to grease the wheels and help out whenever they could.

TABLE OF CONTENTS

Page

LIST OF FIGURES

Figure Page

CHAPTER 1

INTRODUCTION

This dissertation has two main parts: the first part focuses on the motion of particles with translational and rotational velocities and the quantification of their effective diffusivity; the second part focuses on *diffusiokenesis*, the evolution of a nonuniform accumulation of Brownian particles due to a particle diffusivity gradient. The particles concentrate in regions of low diffusivity through an enhanced random walk that requires the presence of bounding walls.

1.1 Motivation

Motion at the microscale is of particular interest because motion at low Reynolds number has some very different defining characteristics compared to the macroscale. As Purcell outlined in his seminal paper "Life at Low Reynolds Number" motion on the microscale is dominated by viscosity (1977). There is no such thing as momentum; or rather it is so small as to be negligible. Once an object quits performing work to propel itself it will instantaneously come to rest. Microorganisms and micromotors are terribly energy inefficient, but they don't have to be. Energy tends to be plentifully available in the environment and the motors only need to move fast relative to their body length (~μm/s). Diffusion becomes a very important effect because not only are length scales shortened but thermal motion can be large relative to the propulsion speed. Synthetic nanomotors have the potential ability to mimic biological motors and perform detailed and specific tasks. In nature this is often accomplished by organisms that are capable of

chemotaxis (the spatially or temporally resolved response to a concentration gradient). The nature of their chemotactic motion is that all properly functioning motors will invariably find their way to region of high or low concentration for chemoattractants and chemorepellents, respectively. Unfortunately no synthetic nanomotors have been developed that are capable of such a precise response to a concentration gradient. However, synthetic motors should be capable of chemokinetic responses.

A chemokinetic response is where the motors concentrate as a result of a bounded random walk in a concentration gradient of some chemical that elicits either a change in the velocity or turning frequency from the motor. A chemokinetic response can be thought of as a bounded random walk in a diffusivity gradient, where the motors end up with a steady state distribution in which the more motors end up in the region of low diffusivity. The motors are not trapped or attracted to the region of low diffusivity but rather they move randomly and can escape the region of low diffusivity, but they on average spend more time in the region of low diffusivity. If the diffusivity gradient is the reason for the chemokinetic accumulation of motors then particles that only move through Brownian motion should also exhibit chemokinesis in a gradient. Chemokinesis is generally considered to be possible only for swimming motors, but the equations that govern their motion also suggest that it should be possible for objects moving only with Brownian thermal motion. Chemotaxis and chemokinesis are important responses for synthetic motors to be able to replicate because it allows for passive of control of a collection of motors. This is very important because in order to perform a significant

amount of work many motors are needed and it is not feasible to direct them individually to areas of need. Passive control is also a useful tool for non-motors for the same reason.

1.2 Literature Review

1.2.1 Chemotaxis and chemokinesis.

Chemotaxis was first discovered as a means of guiding the direction of motion of biological systems by Engelmann (1881). Typically whether or not motors exhibit chemotaxis has been determined by the chemotactic index (CI). The CI is usually determined from an assay where the long-time response is defined as the number of motors in the region of high (low) concentration over the number of motors in the low (high) concentration region for a chemoattractant (chemorepellent). The problem with this type of assay is that it is possible that the global accumulation of the motors is a purely random diffusive type response (chemokinesis). This is a common mistake that people have attempted to correct many times including by Zigmond and Hirsch (1973). However, their method is crude and is only applicable for a specific type of assay.

Part of the answer to how to properly distinguish between chemotaxis and chemokinesis lies in the swimming patterns of the motors. In general there are two distinct types of swimming behavior of synthetic motors, rotationally diffusive swimmers and circle swimmers. Rotationally diffusive swimmers are motors whose translational speed depends on fuel concentration but their rotational motion is governed by Brownian motion. The long-time behavior of these motors is studied in Howse et al. (2007). In this work the authors show that the diffusivity of rotationally diffusive swimmers is governed by their translational velocity squared over their rotational diffusivity. Circle swimmers

have been studied in a number of papers including Ebbens, Golestanian, and Howse (2010), van Teeffelen and Löwen (2008), and van Teeffelen, Zimmermann, Löwen (2009). In these works an initial study of how the nature of the swimming path of circle-swimmers affects their long term behavior. Ebbens et al. created circle swimmers by coupling two individual half coated (in platinum) Janus microspheres, while both works by Teeffelen et al. are for motors with simulated circle swimming behavior.

1.2.2 Chemotaxing biological motors.

Some biological motors can exhibit chemotaxis. For example a human polymorphonuclear leukocyte (neutrophil) and *E. coli* are both designed so that they swim towards high concentration of given chemicals (chemoattractant) or away from a high concentration of a chemorepellent (Zigmond & Hirsch, 1973; Berg & Brown, 1972). The leukocyte will chase down a *Staphylococcus aureus* microorganism by spatially sensing the gradients in chemoattractant emitted by the microorganism (Keller, et al., 1977). On the other hand *E. coli* uses temporal sensing to change its rotational and translational velocity (Berg & Brown, 1972). The behavior of *E. coli* is that of a runner/tumbler. As long as the bacteria senses an equal or increasing chemical concentration gradient it will continue to travel (run) in that direction. When the local concentration begins to decrease *E. coli* enters its' tumble phase and stops moving. The *E. coli* then randomly reorients itself and travels in the new direction in the same manner (Berg, 1975). This is called chemotaxis because all working chemotaxing cells/bacteria will unfailingly find their way to the high concentration of their chemoattractant (Ahmed,

Shimizu, & Stocker, 2010). One of the defining qualities of chemotaxis is that the organism can sense and react directionally to spatial or temporal gradients.

1.2.3 Synthetic motors.

Synthetic nanomotors are being developed to mimic nanoscale biomotors present in biological systems. Efforts in this area range from synthetic modifications on existing biomotors (Brunner, Wahnes, & Vogel, 2007; van den Heuvel & Dekker, 2007; Doot, Hess, and Vogel, 2007; Hess, Bachand, & Vogel, 2004; Goel & Vogel, 2008) to purely synthetic catalytic bimetallic nanomotors (Paxton et al., 2004; Paxton, Sen, & Mallouk, 2005; Fournier-Bidoz, Arsenault, Manners, & Ozin, 2005). Motion of the synthetic motors has been achieved using a number of propulsion mechanisms including auto-diffusiophoresis (Howse et al., 2007; Ebbens, Jones, Ryan, Golestanian, & Howse, 2010; Chaturvedi, Hong, Sen, & Velegol, 2010), auto-electrophoresis (Paxton et al., 2004; Paxton et al., 2005; Dhar et al, 2006; Paxton et al., 2006; Yang et al., 2006), and bubble generation (Manesh et al., 2010; Ismagilov, Schwartz, Bowden, & Whitesides, 2002). There are numerous reviews of motors like Ebbens and Howse (2010) for a general review of motors and to Paxton, Sen and Mallouk (2005) or Wang (2009) for reviews self-electrophoretic motors.

Bimetallic nanomotors have been engineered to swim at 100 body lengths per second as well as pick up, haul, and release micrometer-scale cargo (Burdick, Laocharoensuk, Wheat, Posner, & Wang, 2008; Sundararajan, Lammert, Zudans, Crespi, & Sen, 2008). Their motion can be controlled using external magnetic fields (Burdick et al., 2008; Kline et al., 2006) as well as chemical (Calvo-Marzal et al., 2009; Ibele,

Mallouk, & Sen, 2009; Hong, Blackman, Kopp, Sen, & Velegol, 2007) and thermal (Balasubramanian et al., 2009) fields. Catalytic bimetallic nanomotors propel themselves by electrocatalytically decomposing hydrogen peroxide (H_2O_2) (Paxton et al., 2005; Wang et al., 2006; Moran, Wheat, & Posner, 2010; Moran & Posner, 2011) through a mechanism recently described as reaction induced charge auto-electrophoresis (RICA) (Moran et al., 2010; Moran & Posner, 2011). Bimetallic nanomotors in an aqueous hydrogen peroxide solution catalyze peroxide oxidation at one of the metal surfaces (anode), generating protons, electrons, and oxygen molecules. The electrons conduct through the motor to the other metal surface (cathode) and complete the reduction reaction by combining with protons, peroxide, and oxygen to generate water. The asymmetric reactions result in an excess and depletion of protons in the surrounding electrolyte at the anode and cathode ends, respectively. The proton imbalance results in asymmetric free charge density, which generates an electric dipole and field pointing from the anode to the cathode. In addition, the particle's negative surface charge attracts cations from the bulk solution which form a positively charged diffuse screening layer surrounding the particle. The self-generated electric field couples with the charge density induced by both the reactions and the diffuse layer to produce an electrical body force that drives fluid from the anode to the cathode. The fluid motion results in locomotion of the motor in the direction of the anode. Net motion of the nanomotors requires some native charge, or zeta potential. The nanomotors velocity is linearly dependent on the reaction flux density and the native surface charge (Moran et al., 2010; Moran & Posner, 2011). Most synthetic motors are rotationally diffusive, which means that although the

motors have an advective velocity controlled mainly by some chemical concentration, their orientation is dictated by Brownian fluctuations.

Motors that are fabricated to swim with nonzero mean rotational velocity, ω, in addition to rotational Brownian motion, are capable of more complex motion than rotationally diffusive swimmers. Motors with nonzero mean translational and rotational velocities are classified as circle swimmers (Marine, Wheat, Ault, & Posner, 2013). Circle swimming motors can be fabricated by combining two individual motors (Ebbens et al., 2010) or by growing an additional segment (Gibbs & Zhao, 2009; Gibbs, Kothari, Saintillan, & Zhao, 2011) on the motor such that an asymmetric force profile is generated. Ebbens et al. studied the behavior of these diffusiophoretic Janus doublet particles and noted that the radius of curvature of the circle swimming doublets depends on the respective orientations of the particles within the doublet (Ebbens et al., 2010).

1.2.4 Diffusiokinesis.

The analogue to chemokinesis for non-swimming particles is diffusiokinesis. There is debate in the literature about what happens when particles are in the presence of a diffusivity gradient. Diffusiokinesis has been reported in polymer systems where the diffusivity gradient is generated by changes in polymer conformation (Squires, 2010). Grassia, Hinch, and Nitsche (1995) performed a study based on numerical simulations that suggested that concentrating particles using a diffusivity gradient was impossible. The simulations run with the standard Langevin equations in a variable diffusivity field showed that a concentration could occur but Grassia et al. (1995) determined that such a solution was impossible and the obvious fix was to account for the mass of the particles.

Accounting for the mass in the Langevin equation resulted in uniform distribution of particles at steady state in a diffusivity gradient. Other attempts have been made study the problem including those by Schnitzer (1993) and Visser (2008). In his work Schnitzer derives the Fokker-Planck equation for variable diffusivity in order to study the behavior of *Escherichia coli* (*E. coli*). His approach is based on calculating the flux in two adjacent boxes filled with particles where each box has different diffusivity characteristics. Based on the exact diffusive characteristics it can be determined whether accumulations should be seen in response to a diffusivity gradient. Visser has an alternative derivation that starts from the Langevin equation (2008). The system is then evaluated as a Weiner stochastic process where the diffusivity varies in space. In both cases the Fokker-Planck equation for variable diffusivity contains a parameter α that varies from 0 to 1. The interpretation of this parameter is slightly different in the two cases but in both α serves as a method to account to different collision/turning frequency characteristics of the system and determine if accumulation is possible or not in the system.

1.3 Research Goals and Impact

Here, I present a detailed study of the relevant governing parameters of circle swimming spherical bimetallic catalytic micromotors. I show that there are two important diffusive time scales for these motors and that the relationship between these two diffusivities determines their time average behavior. The motors are fabricated using a technique developed and recently published in Langmuir (Wheat, Marine, Moran, & Posner, 2010). I then demonstrate that passive colloids that migrate only by Brownian thermal motion are also capable of achieving non-uniform pseudo equilibrium

distributions. For Brownian particles the gradient in diffusivity is achieved by creating a viscosity gradient in a microfluidic device. The distribution is described by the Fokker-Planck equation for variable diffusivity. This suggests that any Brownian colloids, natural or synthetic, will concentrate in a bounded system in response to a gradient in diffusivity and that the magnitude of the response is proportional to the magnitude of the gradient in diffusivity divided by the mean diffusivity in the channel.

CHAPTER 2

DIFFUSIVE BEHAVIORS OF CIRCLE SWIMMING MOTORS

2.1 Introduction

In this work, we study the diffusivity of 3 μm spherical catalytic bimetallic circle swimmers over short and long time scales as a function of hydrogen peroxide concentration. We fabricate the motors using multistep metal deposition process on polystyrene microspheres that we reported earlier (Wheat, Marine, Moran & Posner, 2010). We compare the behavior of these motors to Brownian dynamics simulations, simple analytical theory, and to previously published work by Ebbens et al. (2010). The motors exhibit both translational and mean rotational velocities that depend on H_2O_2 concentration. We show that generic circle swimmer motors (not necessarily catalytic motors) exhibit short-time and long-time diffusivities that scale as $v^2/2\omega$ and $v^2/[2D_r(1+(\omega/D_r)^2)]$ respectively. The experimental long-time diffusivities exhibit a maximum diffusivity as a function of concentration because the translational and angular velocities deviate from the linear trend as shown in Figure 5. The deviations are not systematic (i.e. not because the velocity as a function of concentration exhibit some significant nonlinearity). The deviation from the fit is due to natural variation of the swimmer's velocity. We expect that with a larger sample volume or more uniform motors, we may not observe the asystematic variation in velocity that yields the maximum in effective diffusivity, however we provide some simple examples of the conditions under which maximums in effective diffusivities may be observed. Generally, we find that a maximum in long-time effective diffusivity can be achieved in a system

where either v and ω exhibit some nonlinear dependence on concentration (or any other driving potential). Another method by which a maximum in in diffusivity could be achieved is through the modulation of the rotational diffusivity. It is possible to modulate the rotational diffusivity through an unsteady swimming mechanism, as we show in work, or through the curvature of a swimming rod as is shown in Takagi et al. 2013 (Takagi, Braunschweig, Zhang, & Shelley, 2013).

2.2 Theory

2.2.1 Effective diffusivities of swimmers.

The time-averaged displacement of particles with an advective component, such as swimming organisms and the motors described here, can be described by their effective diffusivity. The effective diffusivity combines the effects of rotational diffusion, translational diffusion, and advective motion of the motors. Experimentally, the effective diffusivity can be determined by assembling the mean squared displacement (MSD) of a set of particles and finding the slope. The MSD is determined by taking the ensemble average (to minimize errors due to variability between particles and of individual particles in time) of the squared displacement (SD) of individual particles. The shape of the MSD determines what region the slope is taken for the diffusivity. The MSD is always initially quadratic since the particle must initially move directly away from its origin. Typically the quadratic region transitions into a linear long-time region where the classical diffusivity is the slope divided by 2^n, where n is the number of dimensions over which the displacement is tracked.

The long-time behavior of rotationally diffusive motors was studied by Howse et al. for platinum Janus particles that swim by auto-diffusiophoresis in hydrogen peroxide (Howse et al., 2007). By calculating the MSD of the motors they were able to determine the effective diffusivity of the motors as a function of concentration and show that for rotationally diffusive swimmers the long-time effective diffusivity is (Howse et al., 2007)

$$D_L = D_o + \frac{v^2}{4D_r} \tag{1}$$

where D_o is the Brownian translational diffusivity, v is the velocity of the motor, and D_r is the Brownian rotational diffusivity. From Stokes-Einstein, the Brownian translational diffusivity of a sphere is $D_o=k_BT/6\pi\mu a$ and the Brownian rotational diffusivity is $D_r=k_BT/8\pi\mu a^3$, where k_BT is the thermal energy, μ is the dynamic viscosity of water, and a is the radius of the sphere (Happel & Brenner, 1983). This means that rotationally diffusive swimmers, like catalytic bimetallic nanorods, with considerable advective velocities are capable of achieving effective diffusivities approximately 4 orders of magnitude larger than that of a Brownian particle of the same size (Mirkovic, Zacharia, Scholes, & Ozin, 2010).

For circle swimmers the shape of the MSD can be determined by solving the appropriate Langevin equations. The standard Langevin equations are reduced to 2-D because the motors settle near the surface and are modified such that the displacement of the motors is the sum of its advective and Brownian components as shown in Equations (2)-(4 (Ebbens et al., 2010; van Teeffelen & Lowen, 2008).

$$\frac{dx(t)}{dt} = v\cos\theta(t) + \xi_1(t) \tag{2}$$

,

$$\frac{dy(t)}{dt} = v\sin\theta(t) + \xi_2(t) \tag{3}$$

,

and

$$\frac{d\theta(t)}{dt} = \omega + \zeta(t) \tag{4}$$

.

Where ω is the rotational velocity, x and y are the location of the center of mass, and θ is the orientation of the motors. The Brownian fluctuations terms, ξ and ζ, are Gaussian random variables with zero mean and whose magnitudes are determined from theoretical isotropic Brownian diffusivities. In Ebbens et al. (2010) and van Teeffelen and Löwen (2008) Equations (2-(4 are solved to determine the MSD,

$$\begin{aligned}\Delta L^2(t) = 4Dt + \frac{2v^2 D_r t}{D_r^2 + \omega^2} + \frac{2v^2\left(\omega^2 - D_r^2\right)}{\left(D_r^2 + \omega^2\right)^2} \\ + \frac{2v^2 e^{-D_r t}}{\left(D_r^2 + \omega^2\right)^2}\left[\left(D_r^2 - \omega^2\right)\cos\omega t - 2\omega D_r \sin\omega t\right]\end{aligned} \tag{5}$$

The MSD switches from a sinusoidal short-time region to a long-time region when $t > \pi/\omega$. We term the sinusoidal region the short-time region and we define the short-time diffusivity, D_S, from the slope of the linear region of the first rising wave. Everything that follows the first rising wave is considered the long-time region with a long-time

diffusivity, D_L. As is shown in Ebbens et al. (2010), Equation (5 can be used to solve for the long-time diffusivity of a circle swimmer (Ebbens et al., 2010),

$$D_L = D_o + \frac{v^2}{2D_r\left[1+\left(\frac{\omega}{D_r}\right)^2\right]} \tag{6}$$

Equation (6 shows that the rotational thermal motion modulates the effective long-time diffusivity through the translational and angular velocities. The translational thermal motion, D_o, on the other hand is only additive. A circle swimmer with no rotational Brownian motion swims in a perfect circle with an origin that drifts with D_o and thus will have a long-time effective diffusivity equal to the Brownian translational diffusivity. For a detailed discussion of the interaction between the advective motion and Brownian motion see the Section 2.2.2 and for a detailed discussion of variable rotational diffusivity see Figure 12b.

In order to find the short-time diffusivity we solve Equations (2-(4 assuming that the rotational diffusivity is small compared to the rotational velocity over short times, given as,

$$D_S = D_o + \frac{v^2}{2\omega}. \tag{7}$$

This equation is similar to what we observe for the long-time behavior of rotationally diffusive swimmers (Equation (1) except that the rotational diffusivity is replaced by the rotational velocity. Equation (7 is also similar to Equation (6 except that it scales as v^2/ω

instead of v^2/ω^2 because we assumed the rotational diffusivity to be small in the short-time region. Equation (7 is applicable when the motor has completed less than one half of a rotation or $t<\pi/\omega$. For the range of rotational velocities in this paper the short-time region ranges from 2 s to 120 s.

2.2.2 Circle swimmer MSD evolution.

All Brownian Dynamics simulations shown in the Section 2.2.2 are steady and are performed on a circle swimmer with a mean translational velocity, v=5.32 $\mu m/s$ and a mean rotational velocity of ω=0.3 *rad/s*. **Error! Reference source not found.** shows the mean squared displacement (MSD) for a perfect circle swimmer, i.e. a particle with constant translational and rotational velocity (no Brownian motion or other perturbations to particle motion).

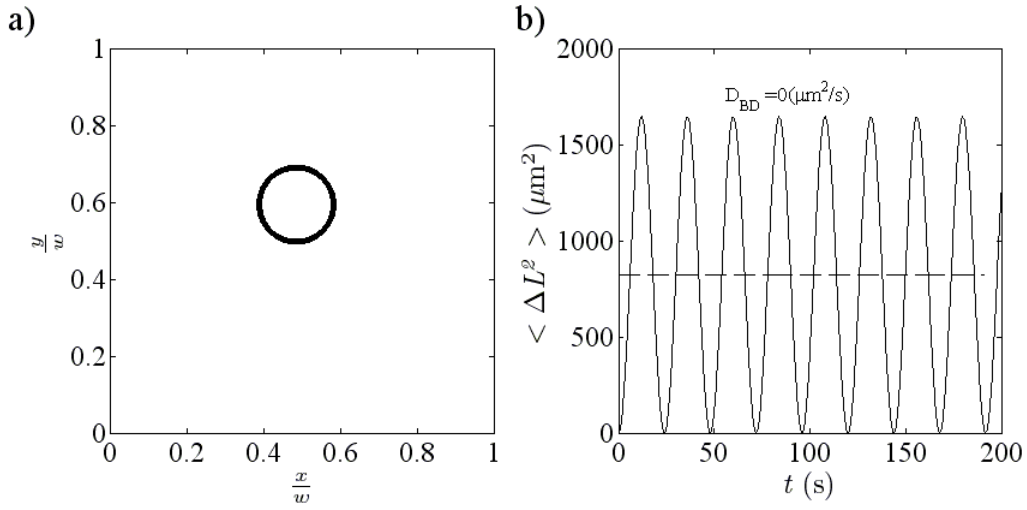

Figure 1. **a)** Trace of a perfect circle swimmer (no Brownian motion). **b)** MSD of a perfect circle swimmer versus time.

The MSD in **Error! Reference source not found.** is a perfect sinusoid and the average slope of the long-time region is zero. Even though the motor has both translational and rotational velocity there is no long-time net motion and the motor swims the same circle repeatedly. The effective short-time diffusivity is given by Equation (7. **Error! Reference source not found.** shows MSD of a circle swimmer with Brownian translational motion but not Brownian rotational motion, i.e. the angular velocity does not vary with time.

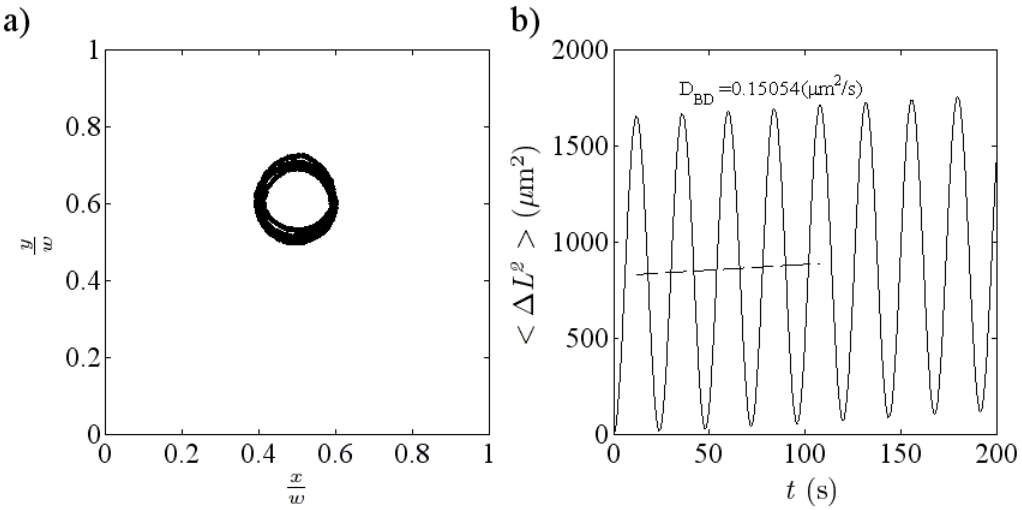

Figure 2. **a)** Trace of circle swimmer with Brownian translational motion but not Brownian rotational motion. **b)** MSD of a circle swimmer with Brownian translational motion but not Brownian rotational motion versus time.

As **Error! Reference source not found.** shows the effective diffusivity, D_{eff}, that is determined from the average slope of the long-time region is the Brownian translational diffusivity, D_o, when a circle swimmer experiences Brownian translational motion but not Brownian rotational motion. The effect is of introducing the Brownian translational diffusivity is that the center of the circle traced by the swimmer drifts over time at the

rate of a Brownian particle of the same size. The effective long-time diffusivity is always D_o regardless of the exact values of the mean translational and rotational velocities. The effective short-time diffusivity is unchanged from the case of the pure circle swimmer. **Error! Reference source not found.** shows the mean squared displacement (MSD) for a circle swimmer that experiences both Brownian rotational and translational motion.

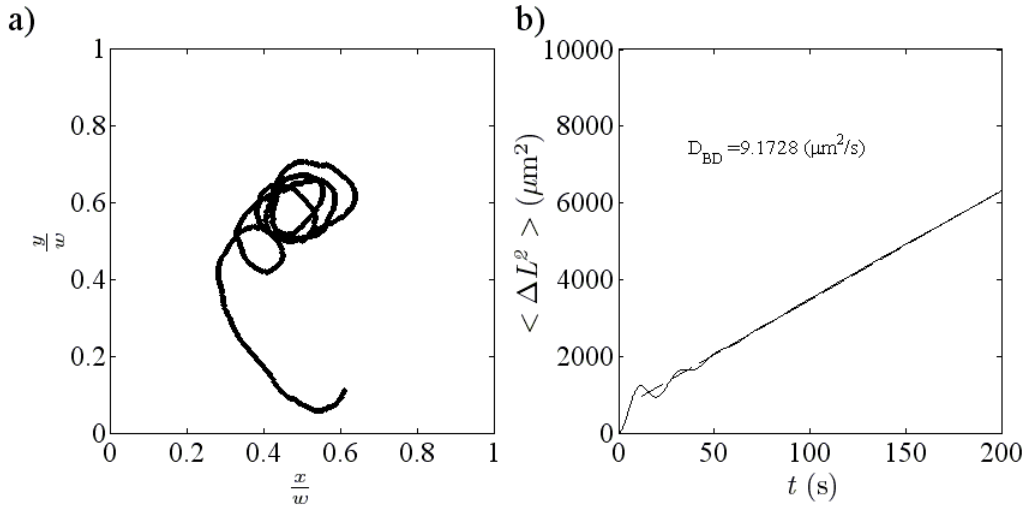

Figure 3. **a)** Trace of circle swimmer with both Brownian rotational and translational motion**. b)** MSD of a circle swimmer with both Brownian rotational and translational motion versus time.

The long-time effective diffusivity of a circle swimmer with both Brownian rotational and translational motion is given by Equation (6. By introducing both Brownian rotational and translational motion the circle changes in size and center of the circle it swims also changes with time. The combination of these effects results in a long-time diffusivity that is orders of magnitude larger than D_o and depends on the mean

translational and rotational velocities of the swimmer. The effect of Brownian rotational motion on the short-time effective diffusivity is small and is shown in Figure 9a.

2.2.3 Velocity and effective diffusivity dependence on concentration.

For particles where the translational and rotational velocities both depend on a third parameter, here fuel concentration, we can rewrite the velocities in terms of that parameter,

$$v(C) = AC^a \tag{8a}$$

and

$$\omega(C) = BC^b \tag{((8b)}$$

Where C is concentration, A (μm/s/M^a), B (rad/s/M^b), and a, b are constants. In this case the short-time diffusivity and long-time diffusivity scale as,

$$D_S \propto C^{2a-b} \tag{9a}$$

and

$$D_L \propto \frac{C^{2a}}{1+C^{2b}}. \tag{9b}$$

Equation (9 predicts that if both the translational and rotational velocities depends linearly on fuel concentration then the short-time diffusivity scales linearly with fuel concentration while the long-time diffusivity increases with concentration and then asymptotes at higher concentrations.

2.3 Experimental Methodology

We fabricate 3μm bimetallic gold and platinum spherical micromotors using a multistep metal deposition process on polystyrene microspheres that we reported earlier (Wheat et al., 2010). In brief, a 1% volume fraction aqueous dispersion of 3 μm

fluorescent polystyrene spheres (ρ = 1.05 g/cm^3, Duke Scientific Inc, Fremont, CA, USA) are deposited onto a 2.5 x 2.5 cm^2 square glass substrate. The solvent evaporates at room temperature, forming a monolayer of spheres. The upper hemispheres are coated with 20 nm of gold using a sputter coater (Cressington 108 auto, Cressington Scientific Instruments, Watford WD19 4BX, England, UK). The half-coated spheres are re-suspended in an aqueous solution and then deposited in random orientations into a monolayer on a clean glass slide. This process is repeated until the spheres are fully coated. The fully Au coated spheres are re-deposited on a clean substrate and coated with 20 nm platinum resulting in a Janus sphere that is half coated with gold and half platinum.

Transmission optical microscopy is used to observe the swimming nanomotors. We use an inverted microscope (Nikon TE2000, Japan) with a 20x objective (NA=0.6) and 100 W halogen illumination (Nikon TE2 PS 100W, Japan). The images are captured using a cooled CCD camera (Cascade Iib, Photometrics, Tucson, AZ). Hydrogen peroxide (Sigma-Aldrich, St. Louis, MO) is used at concentrations of 0.063%, 0.135%, 0.253%, 0.5%, 0.75%, 1.0%, and 1.25% (vol). Experiments are performed in chambered glass wells with an area of 0.4 cm^2 (cat. No. 12-565-110N, Thermo Fisher Scientific Inc., Waltham, MA). During the experiments, the chambers are sealed to prevent evaporation-induced convection. Each motor is tracked for between 100-10,000 frames, and between 20 and 80 different motors are tracked at each concentration. The motors swim only in x-y plane because they settle near the surface and are only tracked when they are far from the sides of the glass well. The positions of the sphere centers are calculated in MATLAB

from the intensity weighted centers of the spheres in each frame. Particle centers at each time are paired using an enhanced PTV algorithm where an optical flow algorithm pairs the particle centers when two particles swim in close proximity. The optical flow algorithm uses the Horn-Schunck global smoothness constraint . Individual particle squared displacements are oversampled before they are averaged into a single mean square displacement. The time averaged velocity and the motor orientation are calculated from the sphere trajectory. The rotational velocity of the motors is calculated from the time averaged displacement of the motors orientation.

We compare the experiments with Brownian dynamics (BD) simulations of spherical circle swimmers in uniform fuel concentration. The simulations are carried out with the modified Langevin equations for 2-D shown in Equations (2-(4 and assume that the standard 2-D Langevin equations are modified such that the displacement of the motors is the sum of its advective and Brownian components (Ebbens et al., 2010; van Teeffelen & Lowen, 2008). The advective velocity of the motors is only in the direction of orientation of the motors and the orientation is governed by a sum of the Brownian and time-averaged rotational velocity. The translational and rotational velocities used in the simulations are from linear fits of the experimental data and the Brownian diffusivities are set to match their theoretical values.

2.4 Results and Discussion

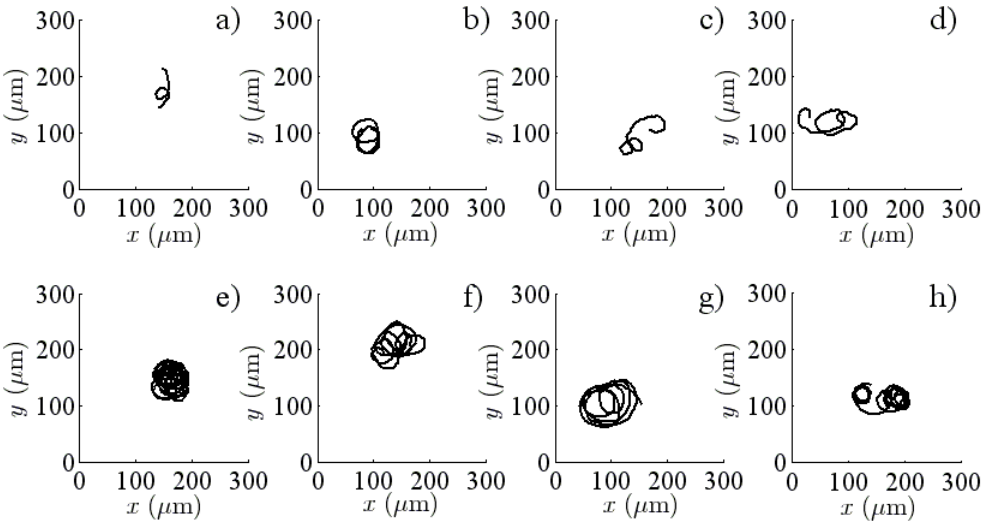

Figure 4. Representative traces of the 3 μm spherical bimetallic motors path over 75 s at each concentration. The hydrogen peroxide concentration increases from a) to h) [0.063 0.135 0.253 0.391 0.5 0.75 1.0 1.25] (volume %).

We previously reported that spherical bimetallic motors swim in H_2O_2 in the same manner as bimetallic nanorods (Wheat et al., 2010). In addition to the translational velocities typical of bimetallic nanomotors, the spherical motors are also observed to possess a rotational velocity. Figure 4 shows representative traces of the 3 μm bimetallic nanomotors at H_2O_2 concentrations of 0.063%, 0.135%, 0.253%, 0.391%, 0.5%, 0.75%, 1.0%, and 1.25% (vol). Each trajectory shows the particle motion for 75 s. These plots show that the motors swim in circular patterns with an advective velocity that increases with the peroxide concentration. The orientation of a motors circular pattern is consistent in time, i.e. a motor that has a clockwise rotational velocity will always trace a clockwise

circular pattern. As we increase concentration (from a to h) we see that the length of the path increases, denoting an increase in translational velocity, and the radius of curvature of the trajectory decreases, denoting an increase in rotational velocity. The motor translational swimming velocities are shown in Figure 5a as a function of the H_2O_2 concentration along with a linear fit of the translational velocity. The translational velocity increases linearly with concentration, which is consistent with previously published data for bimetallic nanomotors in hydrogen peroxide (Paxton et al., 2004; Moran et al., 2010; Moran & Posner, 2011; Wheat et al., 2010; Laocharoensuk, Burdick, & Wang, 2008). The motor angular velocities are shown in Figure 5b as a function of the H_2O_2 concentration along with a linear fit of the angular velocity. The rotational velocity varies linearly with concentration, which is what we would expect if the rotational component was a result of the asymmetric drag profile of the surface of the sphere. As seen in Figure ***5*** of Wheat et al. 2010 the fabrication method results in uneven distribution of mass on the surface of the motors and the extra mass on one side of the sphere results in an asymmetric drag profile of the sphere. The swimming motor would experience a slight spin towards the region of higher drag (the area with extra mass) and the magnitude of the spin would scale linearly with the translational velocity since the drag force scales with linearly with translational velocity at low Reynolds number (Happel & Brenner, 1983). In Figure 5 each error bar represents a single standard deviation. The large standard deviation for both the translational and rotational velocities is high due to the variability between motors.

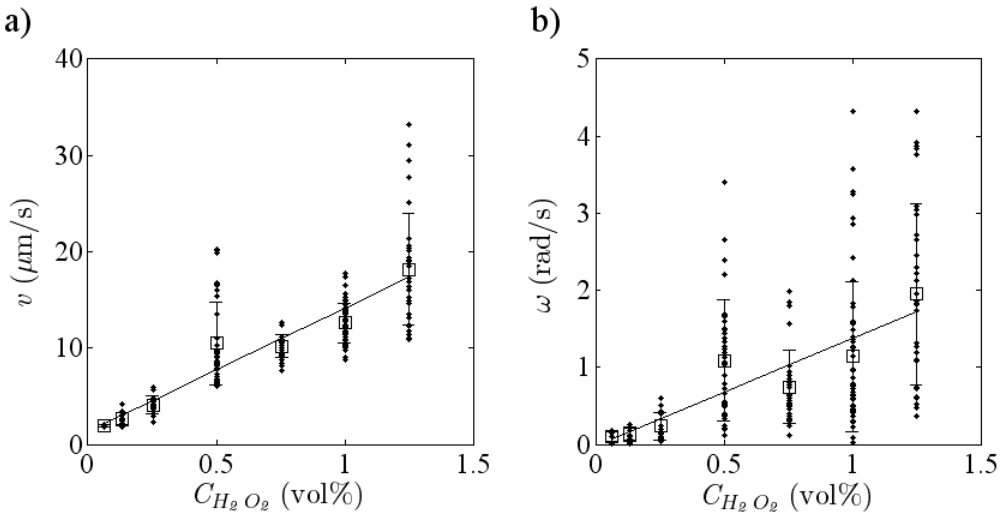

Figure 5. **a)** Average bimetallic spherical micromotor velocity versus hydrogen peroxide concentration. The error bars represent one standard deviation of the ensemble of time averaged velocities. **b)** Average bimetallic spherical micromotor rotational velocity versus hydrogen peroxide concentration. Each individual motor velocity (●) is plotted along with, the mean value (□), and a linear fit of the velocity. The error bars represent one standard deviation of the ensemble of time averaged velocities.

While the translational velocity and rotational velocity describe the motion of the motor at any instant, the effective diffusivity can be used to describe the time averaged behavior. In Figure 6 we show the SDs of three individual motors at H_2O_2 concentrations of 0.135%, 0.253%, and 0.5%. The circle swimmers' SDs exhibit different behavior in short and long time scales (Ebbens et al., 2010; van Teeffelen & Lowen, 2008; van Teeffelen, Zimmermann, & Lowen, 2009). For $t<\pi/\omega$ the SD increases from zero to a local maximum of approximately v^2/ω^2. At long times, $t>\pi/\omega$, the amplitude of the SD exhibits damped oscillations with a frequency that is roughly $\omega/2\pi$. The oscillations at long times are due to the motors swimming in a circular pattern as the center of the circle

drifts away from the origin. The oscillations are damped because the displacement due to advection from the origin becomes large compared to the swimming radius. Each SD in Figure 6 has a different initial local maximum value and occurs at a different time.

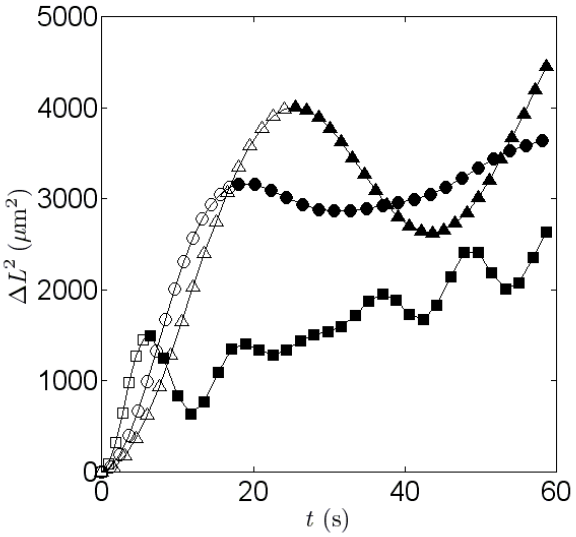

Figure 6. Squared displacement of individual bimetallic spherical micromotors versus time for hydrogen peroxide concentrations of 0.135% (Δ),0.253% (○), and 0.5% (□). For each concentration there is a short time (open symbols) and a long time (filled symbols) diffusivity region. The short time region is marked by the sharp increase of the SD and corresponds to the motor completing half of a rotation. The second region is marked by dampened oscillations that correspond to displacement of the circular motor trajectories.

When the SD shown in Figure 6 is scaled by v^2/ω^2 the SD and time is scaled by π/ω the SD for each concentration will collapse onto a single line for $t<\pi/\omega$ before diverging to their long-time behavior. The data collapse also holds for the MSD as we can see from the Figure 9 where the fit of Equation (7 and the measured short-time diffusivity are in agreement.

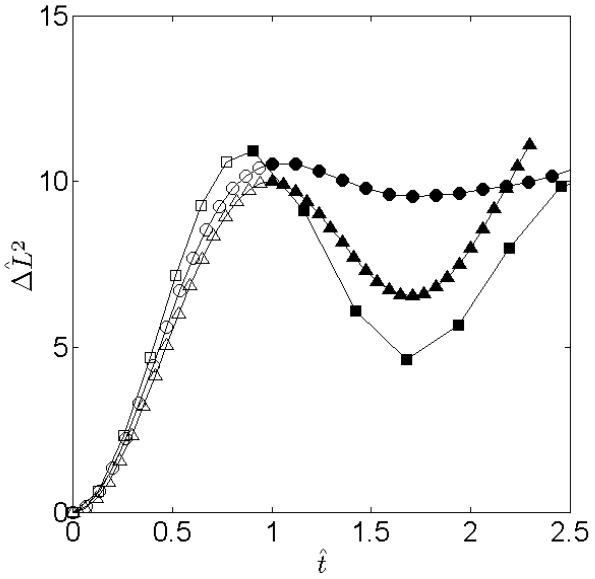

Figure 7. Squared displacement of individual bimetallic spherical micromotors scaled by v^2/ω^2 versus time scaled by π/ω for hydrogen peroxide concentrations of 0.135% (Δ),0.253% (○), and 0.5% (□). For each concentration there is a short time (open symbols) and a long time (filled symbols) diffusivity region. The short time region is marked by the sharp increase of the SD and corresponds to the motor completing half of a rotation. The second region is marked by dampened oscillations that correspond to displacement of the circular motor trajectories.

The SDs of individual motors are shown in **Error! Reference source not found.**7 for H_2O_2 concentrations of 0.5% (a) and 1.25% (b). We can only draw qualitative insights from the SD due to the variability between different motors and the variability of a single motor over a period of time. In order to determine the time averaged motion of these motors as a function of time we can examine the MSD of the ensemble of particles as a function of H_2O_2 concentration.

The MSDs are shown in Figure 8a and 8b at H_2O_2 concentrations of 0.063%, 0.135%, 0.253%, 0.5%, 0.75%, 1.0%, and 1.25%. Each MSD represents an average of between 20 and 80 SDs at each concentration. Figure 8a shows the short-time region,

$t<\pi/\omega$, of the MSD and Figure 8b shows the MSD at each concentration for approximately 150 s capturing both the short-time and long-time regions. In the short-time region shown in Figure 8a, the MSD increases as the swimmers complete half a rotation, consistent with the first phase of a sinusoid. The slope of the linear portion of the short-time region is given by Equation (7) and, as we predict, the slope increases with concentration. The short-time behavior of a circle swimmer is driven by the translational velocity of the swimmer and dampened by the rotational velocity. The long-time behavior of a circle swimmer is shown in Figure 8b. The slope of the long-time region in Figure 8b is described by Equation (6 and has a smaller slope than the short-time region because at long times both the rotational velocity and rotational diffusivity serve to limit net displacement from the origin. The distinct split between short and long time behavior is not observed at lower fuel concentrations because $\omega \sim D_r$ (for a 3 μm sphere in water D_r=0.048 rad^2/s). The experimental MSDs can be compared to theory (using Equation (5 or the BD simulations with the mean experimental velocities). We find that the shape of the MSDs qualitatively agree with Equation (5 in that they both exhibit a short-time behavior that transitions into a long-time region with a lower slope. The magnitude of the MSD slope at short-times (the short time diffusivity) agrees well with Equation (7 as is shown in Figure 9. At longer times, the experimentally measured slope is higher than predicted. The reason for the larger long-time slopes is discussed in detail during the presentation of Figure 10.

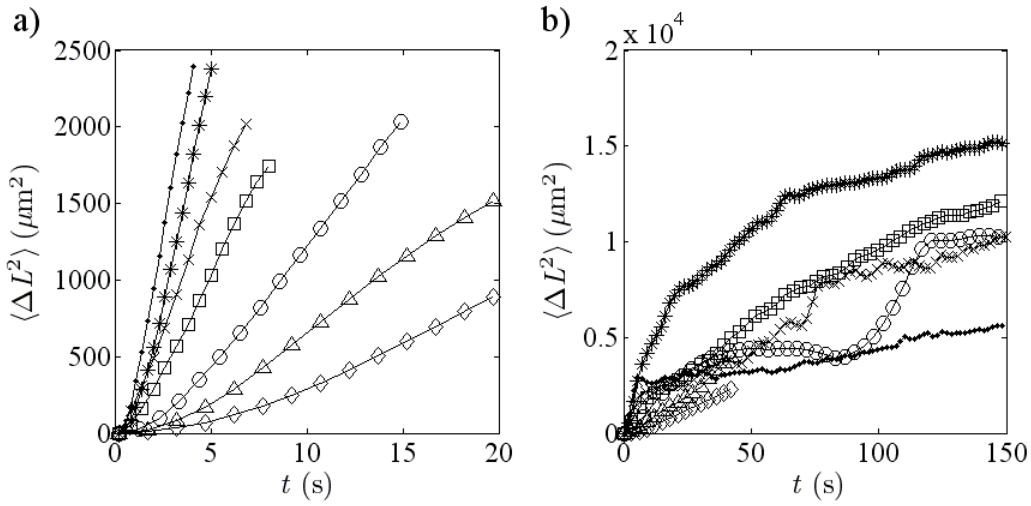

Figure 8. **a)** MSD of bimetallic spherical micromotors versus time for all concentrations of hydrogen peroxide at short times ($t < \pi/\omega$). **b)** MSD versus time at all times. The hydrogen peroxide concentrations shown are: 0.063% (◊), 0.135% (Δ), 0.253% (○), 0.5% (□), 0.756% (x), 1.0% (*), and 1.25% (●). The slope of the MSD gives the effective diffusivity. The slope of the MSD at short times ($t < \pi/\omega$) is the short-time effective diffusivity. The slope of the MSD at long times ($t > \pi/\omega$) is the long-time effective diffusivity.

The largest discrepancy between the Equation (5 and the measured MSD is the MSD magnitude and the time at which the transition between the short and long time behaviors. The theory predicts that this transitions should occur at $t=\pi/\omega$, and have a magnitude of v^2/ω^2, where v and ω are the mean translational and rotational velocities from the average over all of the different motors at a given concentration. The theory and experiments differ in the transition stage of the MSD because the theory assumes all spheres have the mean translational and rotational velocities reported. In the experiments, motors, at any given concentration, exhibit large variations in the ratio of translational to rotational velocity (as revealed large error bars in Figure 10). These variations in

individually measured translational and rotational velocities combined with the relatively small sample size (20-80 separate motors at any given concentration) leads to the discrepancy in height and location of the transition.

From the MSDs shown in Figure 8, we can quantify the short, D_S, and long time, D_L, diffusivities for circle swimmers. In Figure 9 the experimental D_S is plotted along with steady Brownian dynamics simulations with exact experimental velocities, steady Brownian dynamics simulations with velocities determined from linear fits of experimental values, Brownian dynamics simulations with amplified Brownian rotational diffusivities and velocities determined from linear fits of experimental values, and Equation (7 evaluated using fits of the experimentally measured translational and rotational motor velocities. The BD simulations with amplified Brownian rotational diffusivities are BD simulations where the effective rotational diffusivities are increased to $4.5D_r$. All of the plotted diffusivities are scaled by the theoretical Brownian diffusivity of a 3μm sphere in water (D_o=0.145 $\mu m^2/s$).

Figure 9a and 9b show plots of the short-time normalized effective diffusivity as a function of the controlling parameter $v^2/2\omega$ and the H_2O_2 concentration. Figure 9a shows that the short-time effective diffusivity increases linearly with a slope and intercept of unity with the controlling relationship given in Equation (7. In Figure 9a all of the simulations and the experiments agree very well together. The experimental data does show some variation from the theory due to uncertainty in the translational and rotational velocities as well as uncertainty in D_S (due to the relatively small sample size of 20-80

motors at each concentration). From Figure 9a we also see that the theory presented in Equation (7 tends to slightly over-predict the short-time diffusivity because Equation (7 assumes that the effect of the rotational diffusivity is negligible over short-times when the rotational diffusivity actually serves to slightly limit D_S.

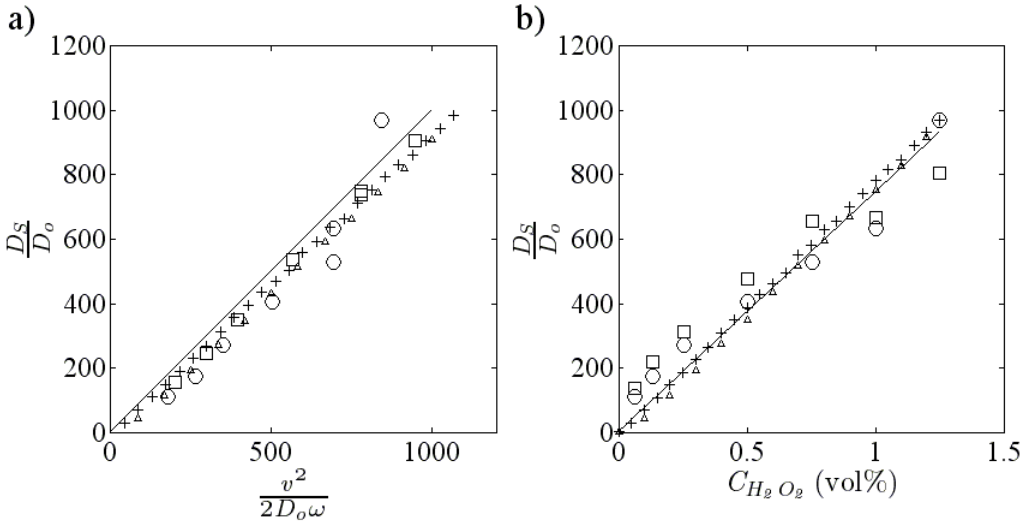

Figure 9. **a)** Short-time effective diffusivity of bimetallic spherical micromotors scaled by Brownian diffusivity versus the controlling parameter, $v^2/2\omega$, scaled by the Brownian diffusivity. **b)** Short-time effective diffusivity of bimetallic spherical micromotors scaled by the Brownian diffusivity versus hydrogen peroxide concentration. The experimental data (○) is plotted along with steady Brownian dynamics simulations with exact experimental velocities(□), steady Brownian dynamics simulations with velocities determined from fits of experimental values(+), unsteady Brownian dynamics simulations with velocities determined from fits of experimental values (Δ), and the fit of Equation (7 (solid line). The short time effective diffusivity is the slope of the MSD at times less than π/ω shown in Figure 8a.

Figure 9b shows that the short-time effective diffusivity also varies linearly with concentration as predicted by Equation (9a since both v and ω vary linearly with H_2O_2 concentration. D_S measured in the experiments and BD simulations with exact

experimental velocities fluctuate about the theoretical solution, while the BD simulations with fits of the velocities agree well with the theory. Figure 9a suggests that the D_S of the experiments and the BD simulations with exact experimental velocities fluctuate about the theoretical solution in Figure 9b due to the deviation of experimental velocity values from the linear dependence. The swimming motion of the motors results in short-time diffusivities that are between two hundred and one thousand times greater than the Brownian diffusivity. However, due to the circle swimming behavior of motors, the short-time diffusivity is smaller than the long-time diffusivity of a rotationally diffusive swimmer like a bimetallic nanorod or a platinum coated Janus particle in H_2O_2 with the same velocity.

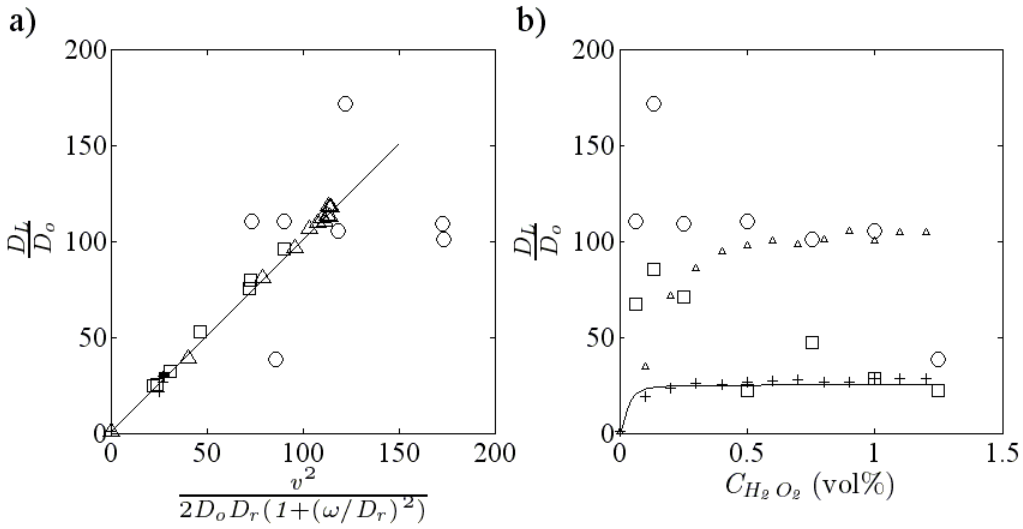

Figure 10. **a)** Long-time effective diffusivity of bimetallic spherical micromotors scaled by the Brownian diffusivity versus the controlling parameter, $v^2/[2D_r(1+(\omega/D_r)^2)]$, scaled by the Brownian diffusivity. **b)** Long-time effective diffusivity of bimetallic spherical micromotors scaled by the Brownian diffusivity versus hydrogen peroxide concentration. The experimental data (○) is plotted along with steady Brownian dynamics simulations with exact experimental velocities (□), steady Brownian dynamics simulations with velocities determined from fits of experimental values(+), unsteady Brownian dynamics simulations with velocities determined from fits of experimental values (Δ), and the scaling shown in Equation (**6** (solid line). The long-time effective diffusivity is the slope of the MSD at times longer than π/ω shown in Figure 8b.

Figure 10a and Figure ***10***b respectively show the long-time diffusivity scaled by D_o as a function of $v^2/[2D_r(1+(\omega/D_r)^2)]$ (from Equation (6) and the fuel concentration for the experimental data, Brownian dynamics simulations with exact experimental velocities, Brownian dynamics simulations with velocities determined from linear fits of experimental values, Brownian dynamics simulations with amplified Brownian rotational diffusivities and velocities determined from linear fits of experimental values, and the theoretical long-time diffusivity given by Equation (6. In Figure 10a the D_L from

Equation (6 shows up as a line with a slope and a y-intercept of unity. The D_L from all of the BD simulations follow the theory, while the experimental D_L shows some scatter. The deviations of the experimentally determined D_L originate from the uncertainty of the translational and rotational velocities. A sensitivity analysis of Equation (6 shows that an uncertainty in the measurement of the translational and rotational velocities of 10% can account for this deviation. It is important to note that in order to collapse all on the diffusivities onto the theory that the appropriate rotational diffusivities of the systems, i.e. for the experiments and for the unsteady BD simulations a rotational diffusivity of $4.5D_r$ was used. Another source for the deviation is the fact that D_L is determined from a heterogeneous population of motors each with their own v and ω that are aggregated into a single D_L value.

In Figure 10b the theoretical solution given by Equation (6 and the steady BD simulations with velocities determined from linear fits of experimental values are in good agreement and suggest that D_L should increase at low concentration before they asymptote to a D_L of roughly a third of the measured D_L at high H_2O_2 concentrations. The measured D_L increases from 0.063% to a local maximum at 0.135% H_2O_2 concentration and then decreases and is relatively constant at high H_2O_2 concentrations, where ω is large compared to D_r. At high H_2O_2 concentrations, $\omega/D_r > 10$, D_L is approximately 100 times higher than D_o but only an eighth of the short-time diffusivity because the long-time diffusivity scales roughly as $v^2/(1+\omega^2)$ instead of v^2/ω. The measured D_L dips at a H_2O_2 concentration of 1.25% due to the trends of the velocities shown in Figure 5, the variability of the motors over a relatively small sample size (47 individual motors at

1.25% compared to thousands for the simulations), and a selection bias in the experimental data. The rotational velocity is 27% higher than expected at a H_2O_2 concentration of 1.25% based on the trend of the rotational velocity at the first six concentrations without a corresponding higher than expected translational velocity. From Equation (6 we can see that this results in a D_L that is 50% lower than expected. The MSD is made up of the average of a group of motors SDs. The shape of the individual SDs is determined by its rotational and translational velocity pair. At 1.25% there is a higher percentage of motors with higher rotational velocities and lower translational velocities (compared to the mean values) than at the other concentrations (look at **Error! Reference source not found.** for individual SDs at 0.5% and 1.25%).

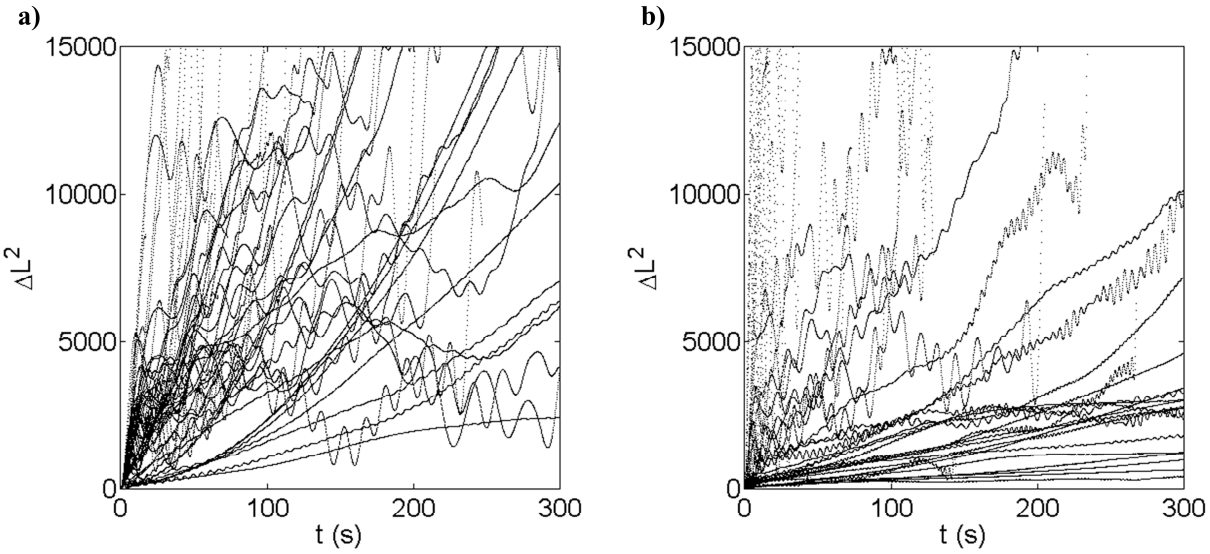

Figure 11. Oversampled squared displacements of individual bimetallic spherical micromotors versus time for hydrogen peroxide concentrations of a) 0.5% and b) 1.25%.

There are 67 individual motors are 0.5% and 47 individual motors at 1.25%. By inspection we can see that 1.25% contains a higher percentage of motors with MSDs that have lower long-time diffusivities, which corresponds to velocity pairs with high rotational and low translational velocities, compared to 0.5%.

This issue is in part due to the relatively small sample size of our data and a small selection bias that is most prevalent at this concentration. The selection bias is due to the fact that motors with a high rotational velocity and low translational velocity tend to stay in the field of view of the microscope (and thus be tracked longer) than motors with high translational velocities and low rotational velocities. This bias becomes more prevalent when the motors, on average, have a high translational velocity. The steady BD simulations with exact experimental values predict a trend similar to that of the experimental data, except that the D_L asymptotes to a value that is roughly a third of the experimentally measured D_L at high H_2O_2 concentrations. The fact that the steady BD simulations and theory all agree on the asymptotic value of D_L at high H_2O_2 concentrations, but the experimental D_L is three times higher suggests that there is an underlying physical mechanism influencing the experiments that is not captured by the steady BD simulations or Equation (6.

In order to understand the discrepancy between the measured and theoretical predictions of the long-time diffusivity in Figure 10b it is useful to examine what parameters contribute to the shape of the MSD (see section 2.2.2). For a perfect circle swimmer, i.e. a particle with constant translational and rotational velocity (no Brownian motion or other perturbations to particle motion or orientations), the average slope of the

long-time region would be zero and the MSD would be a perfect sinusoid. If the circle swimmer were to experience Brownian translational motion but not Brownian rotational motion, i.e. the angular velocity is constant, then the average slope of the long-time region would be the Brownian translational diffusivity D_o. This holds regardless of the translational and rotational velocity supplied by the motors. If the circle swimmer experiences Brownian rotational and translational motion then the slope of the diffusive region is given by Equation (6. For the range of experimental translational and rotational velocities in this paper the addition of rotational Brownian motion results in long-time diffusivities between 50 and 150 times greater than D_o. The reason why the long-time diffusivity that we measure increases one to two orders of magnitude upon the addition of randomness to the orientation of the motors, in this case due to Brownian motion, is because the unsteadiness of the orientation allows for the translational and rotational velocities to take the motor further, on average, from its origin. Therefore, we see that the long-time diffusivity of circle swimmers is strongly modulated by the unsteady orientation of the motors.

We believe that the measured long-time effective diffusivity is greater than the BD simulations and analytical predictions because the unsteadiness of the motors orientation is greater than predicted by the theoretical Brownian rotational diffusivity. This is significant because it illustrates that motors fabricated with unsteady swimming mechanisms will have higher long-time diffusivities than steady motors. For circle swimmers the experimental rotational diffusivity can be calculated from a quadratic fit of the experimental mean squared angular displacement (Ebbens et al., 2010). We observe a

weak linear dependence of the measured rotational diffusivity with concentration with a maximum measured rotational diffusivity of six times what is expected due to Brownian motion at a H_2O_2 concentration of 1.25%. We hypothesize that the increased long-time diffusivity measured in the experiments, as compared to the Brownian dynamics simulations and Equation (6, is due to some additional unsteadiness in the orientation of the motor above what is expected due to Brownian rotational motion. This unsteadiness is potentially driven by fluctuations in the RICA force experienced by the motors. The fluctuations may be due to non-uniform adsorption of anions or other species, intermittent occurrences of the O_2 reduction reactions, or inhomogeneity of H_2O_2 concentration. Regardless of their source, any perturbation to the RICA force (especially the rotational component) causes an increase in the long-time diffusivity. The unsteady perturbations of the RICA mechanism enhance the effective diffusivity in the same way that Brownian rotational diffusivity increases the long-time diffusivity of a perfect circle swimmer. The validity of this assertion can be seen in Figure 10a where we have collapsed the experimental long-time diffusivities around the theory by using an amplified rotational diffusivity. In Figure 10b we include the results of the unsteady simulations (the velocities are based on linear fits of the experimental data) to show that effectively increasing the rotational Brownian diffusivity causes an increase in the motors long-time diffusivity. We make the motor motion unsteady by increasing the magnitude of the Brownian rotational diffusivity to $4.5D_r$ based on our findings from the mean squared angular displacement and from Figure 10a. If the average fluctuation magnitude is held constant with H_2O_2 concentration we observe reasonable agreement of the long-

time unsteady BD simulations diffusivity to the experimentally measured long-time diffusivity at high H_2O_2 concentrations.

Figure 10b shows a local maximum as a function of the concentration in the long-time effective diffusivity for the experiments as well as the BD simulations with exact experimental velocities. This maximum is not predicted from Equation (9b nor observed in the BD simulations with linear fits of the experimental velocities. The observed maximums that occur around peroxide concentrations of 0.135% in Figure 10 are due to a high translational velocity and small angular velocity compared to linear behavior of the translational and rotational velocities at those concentrations. The translational and angular velocities deviate from the linear trend as shown in Figure 5. The deviations are not systematic (i.e. not because the velocity as a function of concentration exhibit some significant nonlinearity). The deviation from the fit is due to natural variation of the swimmer's velocity. We expect that with a larger sample volume or more uniform motors, we may not observe the asystematic variation in velocity that yields the maximum in effective diffusivity. We examine the conditions under which we expect to observe maximums in the long-time effective diffusivity in the next section.

2.5 Maximum of Effective Diffusivity

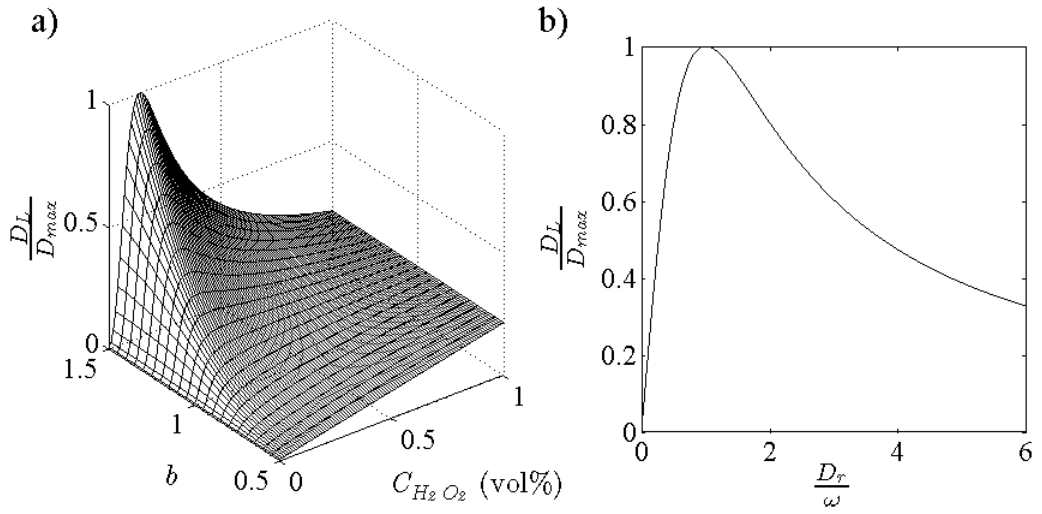

Figure 12. **a)** Space-field map of the normalized long-time effective diffusivity calculated from Equation (**6** as a function of hydrogen peroxide concentration, and order of power dependence of the rotational velocity on concentration ($\omega=K_1C^b$). The long-time diffusivity is normalized by the maximum diffusivity within the sample space. The translational velocity is linearly dependent on concentration for all values of *b*. **b)** The long-time diffusivity calculated from Equation (**6** vs. rotational diffusivity. The diffusivity is scaled by the maximum diffusivity within the sample space and the rotational diffusivity is scaled by the rotational velocity.

The maximum in effective diffusivity observed in the experiments and simulations is a result of asystematic variations in the translational and angular velocity, but we provide some discussion of the conditions under which we might expect to observe a local maximum in effective diffusivity due to systematic velocity dependence on a physical controlling parameter, in this case concentration.

It is instructive to consider a general case, Equation (8, for the dependence of the velocity on a physical controlling parameter, such as concentration, since non-linear

dependencies have been measured (Howse et al., 2007; Gibbs & Zhao, 2009; Kagan et al., 2009; Sabass & Seifert, 2012) and predicted (Howse et al., 2007; Moran et al., 2010; Moran & Posner, 2011; Gibbs & Zhao, 2009) for a variety of motor propulsion mechanisms. Figure 12a shows the contour map of the normalized long-time effective diffusivity calculated from Equation (6 as a function of H_2O_2 concentration, and order of power dependence of the rotational velocity on H_2O_2 concentration, *b,* where the motor's translational and angular velocities can have a nonlinear dependence on the fuel concentration ($v \propto C^a$ and $\omega \propto C^b$ respectively). In Figure 12a, the translational velocity is held linearly dependent on H_2O_2 concentration, $a=1$, for all values of b. As is predicted by the scaling in Equation (9b, when $b \leq a$ Figure 12a shows that D_L increases monotonically and asymptotes at high H_2O_2 concentrations. When $b>a$ D_L increases with concentration to a maximum and decays to an asymptote at high H_2O_2 concentrations. The magnitude of the peak diffusivity increases as the non-linearity of the rotational velocity, b, increases. The maximum occurs when ω increases at a faster rate than v and the rotational velocity dampens the long-time diffusivity at high translational velocities.

Another mechanism by which a maximum in D_L could be achieved is by modulation of the rotational diffusivity. Figure 12b shows the long-time diffusivity as calculated from Equation (6, plotted against the rotational diffusivity scaled by the mean rotational velocity. Modulation of rotational diffusivity has been shown in this work (Figure 10a) and by Takagi et al. (2013). A maximum in D_L is predicted by Equation (6 when the rotational diffusivity equals the rotational velocity. This suggests that there is an optimal amount of randomness in a circle swimmers motion that can maximize its

effective diffusivity. Just enough randomness in the orientation allows the motor to break its' circular trajectory, while too much makes it so that the motor is not able to advect away before reorienting and traveling in a different direction.

2.6 Summary

Spherical catalytic bimetallic micromotors fabricated as described in Wheat et al. (2010) have both translational and rotational velocity that vary with H_2O_2 concentration. The rotational velocity is likely due to asymmetry of the drag profile of the sphere caused by uneven metal coatings in the motor fabrication steps. We show that generic circle swimmer motors (not necessarily catalytic motors) exhibit short and long-time diffusivities that scale as $v^2/2\omega$ and $v^2/[2D_r(1+(\omega/D_r)^2)]$ respectively. The short-time diffusivity is larger than the long-time diffusivity because the long-time diffusivity is proportional to $v^2/(1+\omega^2)$ instead of v^2/ω. $D_S>D_L$ suggests that although a circle swimming motor has a reduced diffusivity at long-times compared to a rotationally diffusive swimmer it samples a much larger region of the space over which it diffuses. The motors transition from short-time to long-time behavior at a time of $\pi/\omega(C)$. Therefore, the governing diffusive time scale varies as a function of hydrogen peroxide concentration. This means that when observed over short-times, or when the motors are confined to small spaces, the motors will appear to have a different diffusivity than at long-times or in large spaces. This effect could result in interesting behavior when a large number of these motors are placed in close proximity because their swimming pattern would lead to a high collision probability.

We also show that artificial swimmers can exhibit maxima in long-time effective diffusivities if the motors have nonlinear translational or rotational velocities, or if the rotational diffusivity is a function the physical controlling parameter, in this work fuel concentration. Here, we do not observe significant nonlinear dependencies of v or ω, and owe the measured maximum in long-time diffusivity to measured translational and rotational velocities that deviate from the expected linear trend at low H_2O_2 concentrations. The combination of diffusive time scales and non-monotonic diffusivity of circle swimming catalytic motors as a function of fuel concentration suggests that we can expect complex particle responses in confined geometries and in spatially dependent fuel concentration gradients.

CHAPTER 3

DIFFUSIOKINESIS

3.1 Introduction

Locomotion of organisms is commonly observed in nature and a key aspect of their transport is the ability to sense and response to gradients of chemicals (chemoattractants and chemorepellents) in a process termed chemotaxis (Berg, 1975). Chemotaxis allows for the directed transport of organism in response to a passive chemical concentration gradient. A chemotactic organism can sense spatial or temporal gradients and uses a feedback to move up or down a chemical concentration gradient. The directional sensing allows chemotactic organisms to concentrate in unbounded systems. Chemokinesis is a similar process to chemotaxis but instead of all of the organisms actively moving towards (away from) the chemoattractant (chemorepellent) they can accumulate in a pseudo-equilibrium distribution where there are more organisms in regions of high chemoattractant or low chemorepellent concentration. The accumulation is a result of a bounded random walk in an imposed concentration gradient of a chemoattractant or chemorepellent that elicits either a change in the velocity or turning frequency from the motor. Organisms are not trapped or attracted to the region of low diffusivity but rather they move randomly and can escape regions of low diffusivity, but they on average spend more time in regions of low diffusivity (Zigmond & Hirsch, 1973; Keller, et al., 1977). A chemokinetic response is often thought of as arising from a gradient in velocity or turning frequency but the most general statement would be that it arises from a gradient in effective diffusivity. Using the diffusivity as a means to describe

an objects motion allows the chemokinetic response to be described by the Fokker-Planck equation for variable diffusivity (Schnitzer, 1993; Visser, 2008). To date, chemokinesis has only been attributed to swimming organisms, but the Fokker-Planck equation for variable diffusivity suggests that it should be possible for any objects that exhibit a spatial diffusivity gradient, even those moving only with Brownian thermal motion.

Grassia, Hinch, and Nitsche (1995) performed a study of particles moving only with Brownian thermal motion in a diffusivity gradient by performing numerical simulations of colloids in different diffusivity gradients using the Langevin equations. The Langevin equations track the displacements of an object based on a drift velocity and a stochastic thermal motion term and describe the underlying physics of the Fokker-Planck equation. Grassia et al. found that the Langevin equations allowed for the concentration in a bounded system. However, when a correction term is added to the standard Langevin equations to account for mass of the particles the concentration gradient of the particles disappeared (Grassia et al., 1995).

In this work we study the response of 2 MDa dextran tagged with Fluorescein (the probe) in a diffusivity gradient (due to a viscosity gradient) generated in a microfluidic device using 10kDa dextran with Texas Red-dextran conjugate tracer. The microfluidic device consisted of parallel top channels, one with water the other with sugar, above a bottom channel filled with the high molecular weight probe. The top layer control channels and the bottom test section channel were separated by a polycarbonate (PCTE) membrane which allowed for the diffusion of the low molecular weight sugar, but no the

high molecular weight probe. The concentrations of the sugar and probe in the bottom channel are measured directly using quantitative fluorescence microscopy. The diffusivity of the probe molecules in different concentrations of sugar is measured using fluorescence recovery after photobleaching (FRAP). The diffusivity of the probe at each point in the microchannel test section is determined empirically from the sugar concentration measured by quantitative epifluorescence the measured diffusivity using FRAP. The measured steady state probe concentration is compared to the Fokker-Planck predictions for variable diffusivity in the empirically extracted diffusivity gradient. The magnitude of the probe concentration gradient is proportional to the strength of the diffusivity gradient and inversely proportional to the mean probe diffusivity in the channel in accordance with the no flux condition at steady state.

3.2 Theory

Diffusiokinesis is a process that takes a gradient in diffusivity and translates it into a concentration gradient. In this work the diffusivity gradient is generated through a gradient in viscosity. The gradient in viscosity is a result of a concentration of sugar. For a gradient device where the control channels (one with sugar, one with water) are separated from a test channel (where the assay takes place) the sugar concentration gradient is determined from Fick's Laws. The concentration of a probe in the test channel is described by the Fokker-Planck equation for variable diffusivity. Both prominent methods for deriving the Fokker-Planck equation for variable diffusivity are discussed here.

3.2.1 Symmetric membrane thickness.

The diffusion of a species through a gradient generating device like those described below is given by Fick's Laws.

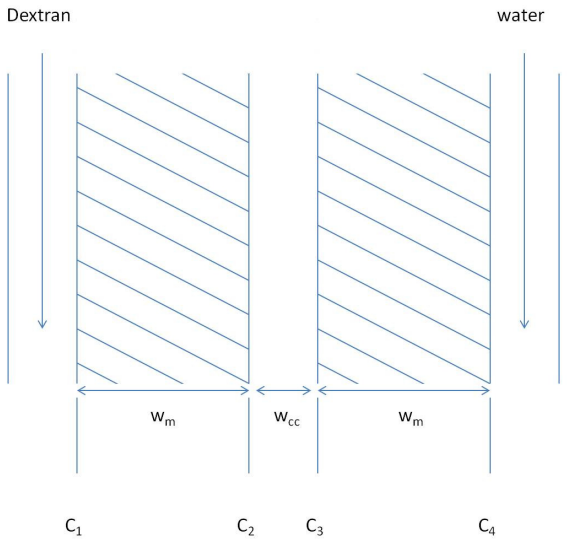

Figure 13. Schematic of a viscosity gradient device with the concentrations at important junction labeled.

The gradient across the center channel (denoted w_{cc} in Figure 13) controls the equilibrium time for the chemokinetic response of the particles to the diffusivity gradient. The gradient across the center channel depends on the thickness of the center channel, the thickness of the membranes, w_m, and the input and output concentrations (C_1 and C_4). The channel used here is approximated as a 1-D concentration problem for the purpose of finding the flux across the channel. 10kDa dextran is flowed in at concentration C_1 through the left channel and pure water through the right channel at C_4=0. Here we are implicitly assuming that the concentration in the left and right channels are uniform despite the diffusion of molecules through the membranes. In order to for this assumption

to be accurate the Peclet number has to be high in the outer channels. This assumption is verified in Section 3.2.3. Fick's First Law (1-D) requires that the flux, *J*, across the channels is constant at steady state

$$J = AD\frac{\partial C}{\partial x}, \tag{10}$$

where *A* is the cross-sectional area of the membrane, *D* is the diffusivity of the dextran, and *C* is the concentration of the solute (dextran). If it is assumed that the concentration gradients are linear, the flux is

$$\frac{ADH}{w_m}(C_1 - C_2) = \frac{AD}{w_{cc}}(C_2 - C_3) = \frac{ADH}{w_m}(C_3 - C_4). \tag{11}$$

In the terms for the flux across the membranes we have introduced the partitioning coefficient of the solute into the membrane, *H*. The partitioning coefficient is used to account for the affinity of the diffusing solute, in this case dextran, for the membrane (Cussler, 2009). A general solution can be attained by writing Equation 11 as a system of equations.

$$\frac{ADH}{w_m}(C_1 - C_2) = \frac{AD}{w_{cc}}(C_2 - C_3), \tag{12}$$

$$\frac{AD}{w_{cc}}(C_2 - C_3) = \frac{ADH}{w_m}(C_3 - C_4), \tag{13}$$

and

$$\frac{ADH}{w_m}(C_1 - C_2) = \frac{ADH}{w_m}(C_3 - C_4). \tag{14}$$

Note that only two of these equations are unique (as can be proved by performing Gaussian row reduction). If the input and output concentrations are known, C_1 and C_4

respectively, then the system can be solved for C_2 and C_3. If C_4=0, which is what is specified by the experimental conditions, the solution is given by Equations (**15** and (**16**.

$$C_2 = \frac{w_m + Hw_{cc}}{2w_m + Hw_{cc}} C_1, \tag{15}$$

and

$$C_3 = \left(1 - \frac{w_m + Hw_{cc}}{2w_m + Hw_{cc}}\right) C_1. \tag{16}$$

Equations (**15** and (**16** show that even if the thickness of the membrane goes to infinity, at steady state C_2 and C_3 both approach 50% of C_1. This case obviously would result in zero gradient across the center channel. Therefore, the maximum gradient across the center channel is achieved when the membrane thickness is small compared to the center channel width. In the limit of $H \rightarrow 0$ C_2 and C_3 both approach 50% of C_1. This makes sense since making w_m large or H small has the effect of hindering diffusion in the membrane.

3.2.2 Asymmetric membrane thickness.

It may be desirable to have membranes with two different thicknesses. Here we resolve the flux equations when the left membrane is w_{m1} and right membrane is w_{m2}. Again we start with Fick's First Law:

$$\frac{ADH}{w_{m1}}(C_1 - C_2) = \frac{AD}{w_{cc}}(C_2 - C_3) = \frac{ADH}{w_{m2}}(C_3 - C_4). \tag{17}$$

Equation 17 is the same as Equation 11 except that w_m has been replaced with w_{m1} and w_{m2}. For this system C_1 is a known input and C_4 is zero. Equation 17 is broken into

$$\frac{ADH}{w_{m1}}(C_1 - C_2) = \frac{AD}{w_{cc}}(C_2 - C_3), \tag{18}$$

$$\frac{AD}{w_{cc}}(C_2 - C_3) = \frac{ADH}{w_{m2}}(C_3 - C_4), \tag{19}$$

and

$$\frac{ADH}{w_{m1}}(C_1 - C_2) = \frac{ADH}{w_{m2}}(C_3 - C_4). \tag{20}$$

Solving the system of equations C_2 and C_3 are determined to be:

$$C_2 = \frac{Hw_{cc} + w_{m2}}{Hw_{cc} + w_{m1} + w_{m2}} C_1 \tag{21}$$

and

$$C_3 = \left(1 - \frac{Hw_{cc} + w_{m2}}{Hw_{cc} + w_{m1} + w_{m2}}\right)\frac{w_{m2}}{w_{m1}} C_1. \tag{22}$$

When $w_{m1}=w_{m2}$ then the solution reduces to Equations 15 and 16. If the membrane thicknesses can be controlled independently the largest resolution, the largest drop in concentration across the channel, occurs when the thickness of the right membrane is small compared to the left.

In the simplest sense the diffusion of a molecule through a membrane can be thought of as hindered diffusion where the expected diffusion is multiplied by some factor that is less than one. This is the approach used in Equation 11, when the partitioning coefficient is added to Fick's First Law. If there was no hindrance factor for diffusing across the membrane the diffusion time across a membrane can be approximated as $t \approx \frac{w_m^2}{2D}$ where w_m is the thickness of the membrane, t is the time required, and D is the diffusivity of the species of interest. The time given by this calculation would underestimate the time required to diffuse through the membrane. A

closer approximation of the time required would be to divide this time by the partitioning coefficient.

3.2.3 Diffusion in the outer channels (Peclet number).

The Peclet number in the outer channels is defined as $Pe = \frac{UL}{D}$. The Peclet number is the ratio between convective and diffusive transport. U is the velocity in the channel, L is the characteristic length scale (here w_{cc}), and D is the diffusivity of the background dextran. When the Peclet number is much larger than unity, the convection of the fluid is so large compared to diffusion so the concentration of the species of interest in the fluid is relatively constant along the length, width, and height of the channel. When the Peclet number is much less than one, diffusion dominates and the concentration of the species of interest decreases along the length of the channel as the species diffuses out of the channel. For this experiment the species of interest is 10 kDa Dextran that has a diffusivity of approximately 115 $\mu m^2/s$ (Armstrong, Wenby, Meiseman, & Fisher, 2004). A syringe pump is used to maintain a flow of 5 μL/hr in the outer channels. The average velocity in the channel is calculated based on the flow rate and the cross sectional area of the top channels. Using the L=15 mm (the length of the channel) we see that this results in a Pe≈400. This suggests that our assumption that the concentration is uniform in the outer channels is valid.

3.2.4 1-D Fokker-Planck equation for variable diffusivity.

There are a number of derivations of the Fokker-Planck equation for variable diffusivity. Schnitzer (1993) derived the Fokker-Planck equation for variable diffusivity

in order to study the behavior of *Escherichia coli*. His approach is based on calculating the flux in two adjacent boxes filled with particles where each box has different diffusivity characteristics. The net flux in the system yields a modified form of Fick's first law from which the Fokker-Planck equation can be derived. Visser has an alternative derivation that starts from the Langevin equation (2008). The system is then evaluated as a Weiner stochastic process where the diffusivity varies in space. In both cases the Fokker-Planck equation for variable diffusivity contains a parameter α that varies from 0 to 1. The interpretation of this parameter is slightly different in the two cases but in both α serves as a method to account for different collision/turning frequency characteristics and determine if accumulation is possible or not in the system. The Fokker-Planck equation for variable diffusivity using the Visser notation is

$$\frac{\partial \rho}{\partial t} = (1-\alpha)\frac{\partial}{\partial x}\left(\rho \frac{\partial D}{\partial x}\right) + \frac{\partial}{\partial x}\left(D \frac{\partial \rho}{\partial x}\right) \tag{23}$$

where, ρ can be interpreted as either the probability density or the concentration and D is the diffusivity of the species at any point in space. When α is one there is no accumulation in response to diffusivity gradient. If α is any other value a species is expected to concentrate in response to a gradient in its diffusivity. The closer α is to unity the more strongly the species concentrates in response to the same diffusivity gradient. Typically the value of α is determined from the experimental data. The other important requirement for achieving a species concentration is the presence of bounding walls. Even with a nonzero α there is no steady state concentration without the no-flux conditions at the boundaries. This is because the concentration is not the result of directed

motion of the species but rather a response to the modified characteristics of the random walk. In an unbound system the particles would ultimately diffuse throughout the infinite domain resulting in a zero concentration everywhere at long times. The species are constantly undergoing a random walk but the average speed with which they move varies with space. Therefore, molecules tend to spend more time in regions of low diffusivity than they do in regions of high diffusivity. However, they are not trapped in any given region and move freely between the two. Steady state is reached when the net flux in the system is zero, i.e. for every molecule that enters the high diffusivity region another particle exits. The SS condition is reached when the net flux is zero, $J=0$, and can be written as,

$$-J = D\frac{\partial \rho}{\partial x} + (1-\alpha)\rho\frac{\partial D}{\partial x}. \tag{24}$$

This condition also describes the strength of the concentration of molecules in response to a given diffusivity gradient. The first flux term is the standard form of Fick's law, when α=0, and represents the tendency of the probe diffusivity to smooth the probe concentration. The second flux term represents the concentrating power of diffusivity gradient.

3.2.5 Simulations of Brownian diffusion in a viscosity gradient.

We perform two simulations of Brownian particles in a viscosity gradient, namely Brownian dynamics and the solution of the modified Fokker-Plank equation. The Brownian dynamics simulations are based on the Langevin equations where the average magnitude of the Brownian kicks is a function of the location in the channel. The sample

space is bounded by elastic reflective walls. The input average diffusivities and shape of the diffusivity gradient are taken from fits of the experimental data. It is verified that the Brownian dynamics solutions give the same solutions as the Fokker-Planck equation for variable diffusivity.

The Fokker-Planck equation for variable diffusivity, Equation (23), is solved numerically using a forward time center space (FTCS) scheme. For this condition a 1-D channel where $0 \le x \le L$, the 1-D modified Fokker-Planck Equation becomes

$$\frac{\partial \rho}{\partial t} = D\frac{\partial^2 \rho}{\partial x^2} + (2-\alpha)\frac{\partial \rho}{\partial x}\cdot\frac{\partial D}{\partial x} + (1-\alpha)\rho\frac{\partial^2 D}{\partial x^2} \tag{25}$$

where ρ is the probability density of the particles occurring at any location, D is the diffusivity of the particle at any location, x is the dimension across the channel, and t is time. The boundary conditions (BCs) for this system are that there is no flux of particles at the boundaries. The BCs are shown in Equation (26

$$J = \left[-(1-\alpha)D\frac{\partial \rho}{\partial x} - \rho\frac{\partial D}{\partial x}\right]_{x=0} = 0, \tag{26a}$$

and

$$J = \left[-(1-\alpha)D\frac{\partial \rho}{\partial x} - \rho\frac{\partial D}{\partial x}\right]_{x=L} = 0. \tag{26a)b}$$

The numerical discretization of Equation (25 after applying FTCS is

$$\rho_i^{n+1} = \rho_i^n + \Delta t\left[\begin{array}{l} D_i\dfrac{\rho_{i+1}^n - 2\rho_i^n + \rho_{i-1}^n}{\Delta x^2} + \ldots \\ \ldots + (2-\alpha)\dfrac{\rho_{i+1}^n - \rho_{i-1}^n}{2\Delta x}\dfrac{D_{i+1}^n - D_{i-1}^n}{2\Delta x} + (1-\alpha)\rho_i^n\dfrac{D_{i+1}^n - 2D_i^n + D_{i-1}^n}{\Delta x^2} \end{array}\right] \tag{27}$$

where *i=1:Nx* and *n=1:Nt*. This method is first order accurate in time and second order accurate in space. For a FTCS scheme on the unmodified Fokker-Planck equation there is a stability condition such that

$$\frac{D\Delta t}{\Delta x^2} \leq \frac{1}{2}. \tag{28}$$

Fokker-Planck equation for variable diffusivity does not possess a simple stability condition due to the extra terms in the PDE and the fact that the diffusivity varies with space. Here we choose the most stringent condition for Δt based on Δx to achieve stability (i.e. we choose the minimum diffusivity in the system).

The BCs for Equation (27 require special attention because if applied improperly or without proper fidelity they will result in rapid mass loss from the solution when a gradient in diffusivity is present. Therefore, it is not recommended to use a first order method like a forward or backward space discretization at the boundaries. A second order centered difference scheme by utilizing ghost points can be used at the boundaries. However, since the BCs can also be solved analytically it makes sense to use the exact solution. Applying separation of variables to Equation (26a) we get

$$C_1 = C_2 \frac{D_2}{D_1\left(1-\alpha\right)}, \tag{29a}$$

and

$$C_{Nx-1} = C_{Nx} \frac{D_{Nx}}{D_{Nx-1}\left(1-\alpha\right)} \tag{29b}$$

at all time steps.

3.2.6 Diffusiophoresis in non-electrolyte gradients.

For chemokinetic experiments there is a concern that the observed response of the probes is not due to non-directed accumulation in a diffusivity gradient and instead is a diffusiophoretic drift velocity to the concentration gradient of the background molecules used to generate the diffusivity gradient. From Anderson (1989), we know that the diffusiophoretic velocity that arises from a concentration gradient for uncharged solutes is

$$U = \frac{kT}{\mu} K L^* \nabla C \tag{30}$$

where, U is the diffusiophoretic velocity, kT is the thermal energy, μ is the dynamic viscosity, K is the Gibbs absorption length, and L^* is the characteristic length of the particle-solute interaction. Due to limits in the theory for polymer-polymer interactions the exact diffusiophoretic velocity is unknown. However, from Anderson (1993) and Staffeld and Quinn (1988) the diffusiophoretic velocity can be minimized by choosing a solute (10 kDa dextran) that is small, with low polarizability, the channel width should be as large as feasible, and there should be a background buffer that minimizes the double layer thickness of solute molecule and probe molecules.

3.3 Experimental Methodology

A device in which diffusiokinesis can be measured has a variety of requirements. It has to be able to generate diffusivity gradient, the system has to be bounded in diffusivity gradient direction, there can be no pressure driven flow in test channel, the diffusivity gradient has to be strong enough to elicit a measureable response, and the

solutes must be chosen so that the potential sources of drift velocities (diffusiophoresis, gradients in potential) are minimized.

3.3.1 Gradient generating devices.

Chemotaxis of bacteria, cells, and other microorganisms is studied in a variety of different devices. Generally, the devices work by placing the microorganisms of interest in between a source (a chemoattractant or chemorepellent) and a sink (absence of the chemoattractant or repellent). One of the most basic devices utilizes a Y-shaped microchannel where the gradient is setup up by running the source and sink in parallel in the channel that also contains the microorganism (Abhyankar, et al., 2008; Long & Ford, 2009). Another common method utilizes agarose gel as a membrane in between the source, the microorganisms and the sink (Ahmed, Shimizu, & Stocker, 2010). Recently we have studied the chemokinetic response of synthetic bimetallic nanorods using a steady-linear-concentration gradient generator of the design first introduced by Diao et al. in 2006 (Palacci et al. 2010; Haessler et al. 2009; Wheat, Marine and Posner, 2013). The design requires channels to be cut into a nitrocellulose membrane with a laser. There are issues with using each type of device. The Y-shaped microchannel devices require the microorganism of interest to be able to stick to the channel so that they don't advect away with the solutions or that the chemotactic response time is less than the time it takes the organisms to advect down the channel. The agarose gel membranes tend have limited pore size options and are therefore limited in what may diffuse through them. The nitrocellulose membrane thickness tends to be very large due to the thickness of the laser. As is shown in Section 3.2.1 this has the effects of reducing the gradient across the

channel compared to when the membrane thickness is small. The other issue is that when using larger molecules the tortuosity of the membranes results in a very low partitioning through a thick membrane.

3.3.2 Device fabrication.

The gradient generating device used in these experiments is shown in **Error! Reference source not found.**. It is a multilayered structure consisting of top control channels and a bottom test channel that are separated by a microporous membrane. Water is flown through one control channel while sugar is flown through the other. The sugar is free to diffuse through the membrane into the test-channel and across and out the other side to test-channel, through the membrane and out through the water filled control channel. The probe molecules, 2MDa dextran, are too large to diffuse through the membrane and the channel-wise flow is stopped by controlling the height of water in the inlet and outlet wells so that the probes only move through diffusion.

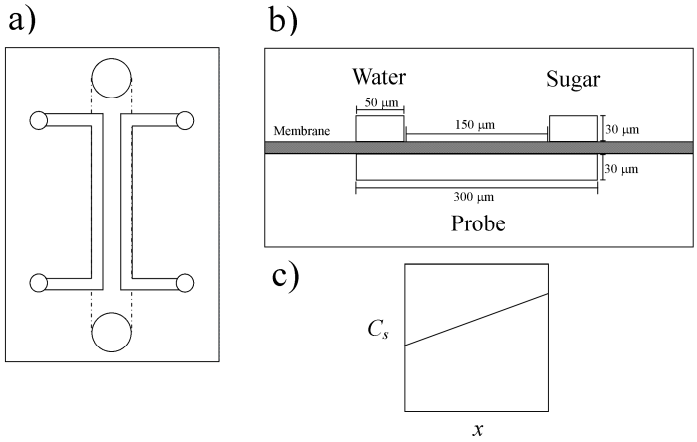

Figure 14. Schematic of the structure used to generate steady-linear chemical concentration gradients for the chemokinesis assays. The control (top) channels are 50 μm wide and 30 μm deep and are separated by a gap of 150 μm. The test (bottom) channel is separated from the top by a polycarbonate membrane (with 30 nm cylindrical pores, thickness of 6-15 μm) and is 300 μm wide and 30 μm deep. Water is flown through one top channel while sugar is flown through the other. The sugar is free to diffuse through the membrane while the probe molecules are trapped in the bottom channel. a) Top view of the channels. b) Side view of the device. c) The steady state sugar concentration gradient in between the control channels.

The test channel is 300 μm wide and 30 μm deep and the control channels are 50 μm wide and 30 μm deep. The distance between the inner edges of the top channels is 150 μm which results in partial overlap of the control and test channels. This overlap was retained in order to facilitate the alignment of the top and bottom sections. Alignment is done by hand with the aid of a stereo microscope and without play in the alignment allowed by the overlap the device yield was too low. The top and bottom channels were fabricated using soft lithography of PDMS (Duffy, McDonald, Schueller, & Whitesides, 1998). We use an SU8 (2025 MicroChem. Corp., Newton, MA) master template fabricated on a Si (100) wafer (University Wafer Corp., Boston, MA) using photolithography. Sylgard 184 PDMS prepolymer (Dow Corning, Midland, MI) at 10:1

base polymer/curing agent (A:B) is then cast on a silanized master. The PDMS is then cured at 80° C in a convection oven for 30 min. The individual structures are bonded to the membrane using the process described by Aran, Sasso, Kamdar, and Zahn (2010). The membranes are made out of polycarbonate, have 30 nm diameter cylindrical pores, and are 6-15 μm thick (CAT# PCT00325100, Sterlitech Corp., Kent, WA). The membranes are first activated in an oxygen plasma chamber (600 mTorr, 100 W) for 1 min and then immersed in a solution of 3-amino-propyltriethoxysilane (APTES) (CAT# A3648, Sigma-Aldrich, St. Louis, MO), diluted in water to 5% by volume, at 80° C for 20 min. The APTES solution is heated on a hot plate and covered so that the water does not evaporate. The soaked membranes are removed with tweezers and placed on a cleanroom wipe to dry. The dried membrane is then brought into contact with PDMS structures that have been activated in the oxygen plasma chamber (600 mTorr, 100 W) for 30 s.

3.3.3 Solution preparation.

Sugar stock solutions of 10 kDa dextran (CAT# D9260, Sigma-Aldrich, St. Louis, MO) were prepared at concentrations of 0.045, 0.09, and 0.18 g/mL. The stock solutions are combined with 10kDa dextran conjugated with Texas Red (CAT# D1828, Invitrogen, Carlsbad, CA) such that the final total concentrations of 10kDa dextran are 0.032, 0.062, and 0.122 g/mL (~0.0122 M) and the concentration of Texas Red conjugated 10kDa dextran is 2.18 mg/mL for all three solutions. The probe solutions are 2MDa dextran conjugated with Fluorescein (CAT# FD2000S, Sigma-Aldrich, St. Louis, MO) at a concentration of 2 mg/mL. The FRAP solutions consist of the untagged 10 kDa dextran

at concentrations of 0.009375, 0.01875, 0.0375, 0.075, and 0.15 g/mL each with 2 MDa dextran conjugated with fluorescein at a concentration of 2 mg/mL. The approximate concentration of Fluorescein is 10 nM.

3.3.4 Imaging and flow conditions.

We used quantitative epifluorescence microscopy on an inverted microscope (TE 2000, Nikon, Melville, NY) with a 40 x objective (NA=0.5) to image the variable diffusivity experiments. Images were recorded on a 12 bit, high speed CMOS camera (Phantom v12.1, Vision Research, NJ 07470, USA) at a resolution of 800 x 600 pixels and an exposure time of 10 ms. The fluorescence intensity of the Fluorescein tagged probe is imaged with a blue-green filter cube (Excitation 450-490nm, Emission 510-570nm, XF100-2, Omega Optical, Brattleboro, VT), while the Texas Red tagged tracer is imaged with a green-orange filter cube (Excitation 508-545nm, Emission 573-633nm, XF108-2, Omega Optical, Brattleboro, VT). A syringe pump (KD Scientific Model 210, Holliston, MA) is used to drive the flow in the control channels at a speed of 5 μL/hr to provide constant inlet and outlet concentrations of the sugar and water (Pe≈400). The solutions are driven in glass 50 μL syringes (Fisher Scientific, Waltham, MA) with fluidic connections made using Tygon tubing (1/16'' ID, McMaster-Carr, Santa Fe Springs, CA) and stainless steel tubes (NE-1300-01, New England Small Tube Corp., Litchfield NH). The flow in the test channel is controlled by varying the water height in the well at each end of the channel. Before measuring concentration of the probe in the diffusivity gradient the solution in the bottom channel is flushed so that there is no initial

probe concentration gradient and sugar concentration gradient. After the fresh solution is flushed through the flow is again stopped.

3.3.5 Imaging and data processing.

For each experiment the flatfield and dark-field images are recorded for each solution at the locations in the channel where data will be taken. For both of the dark-field images the fluorescence intensity is measured with only buffer in the channels. For the probe flatfield the control channels are filled with water and the test channel is filled with the probe solution. For the 10 kDa dextran tracer flatfield, both of the control channels and the test channel are filled with 10 kDa dextran solution to be used in the experiment. The flatfield and dark-field images are then used to correct the images taken during the experiment to gain the scalar concentration using Equation (31

$$\frac{C(x,y)}{C_o} = \frac{I(x,y)_{raw} - I(x,y)_{dark}}{I(x,y)_{flat} - I(x,y)_{dark}}. \tag{31}$$

Where C is the concentration of measured fluorescent molecule, C_o is the input concentration, I, represents the temporal average of ten consecutive frames, and the subscripts *raw*, *flat* and *dark* denote the raw, flat, and dark-field images respectively. After the flatfield and dark-field corrections the corrected concentrations are averaged axially to form the line plots.

3.3.6 Concentration vs. fluorescence intensity for FITC dextran.

The linearity of the intensity of the different tagged dextran solutions have been verified for all of the solutions used in this dissertation. Figure 15 shows the concentration versus fluorescence intensity of 10kDa FITC tagged dextran.

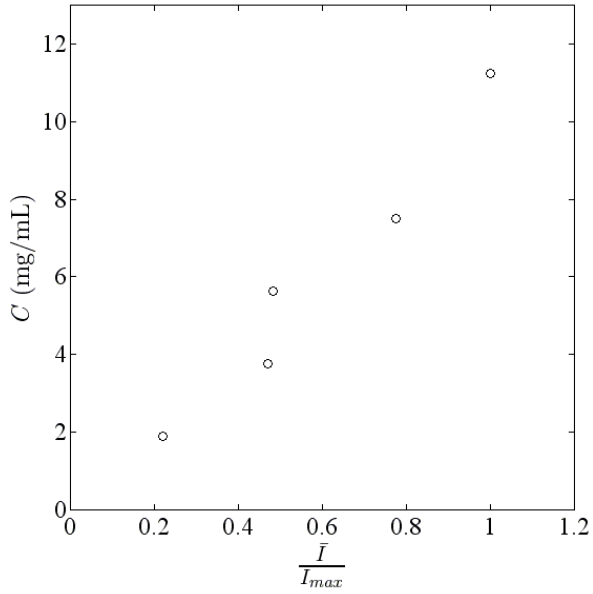

Figure 15. The concentration of 10kDa dextran tagged with FITC versus their normalized fluorescence intensities.

Figure 16 shows the concentration versus fluorescence intensity of 2MDa FITC tagged dextran.

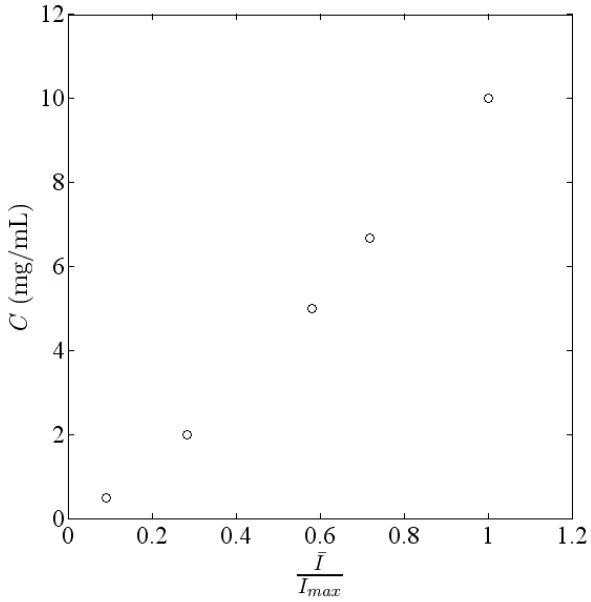

*Figure 16.*The concentration of 2MDa dextran tagged with FITC versus their normalized fluorescence intensities.

3.3.7 Fluorescence recovery after photobleaching (FRAP) theory.

In 1976 Axelrod, Koppel, Schlessinger, Elson, and Webb demonstrated how photobleaching a molecule could be used to calculate its diffusivity. A laser scanning confocal system is used to bleach a small region of the field of view of a microscope. The region that is bleached is saturated with light until the area no longer fluoresces because all of the excitable electrons have moved to a lower energy state, leaving the region dark. The recovery of the intensity of the region as unbleached dye from elsewhere in the system diffuses in is then monitored. The intensity of the dye is correlated to the concentration of the dye. The theoretical recovery profile at any given time can be calculated from the advection-diffusion equation. The exact solution depends on the shape of the bleached region, which depends on the profile of the laser beam used for the

photobleaching. Axelrod et al. (1976) outlined a solution method for a circular region with a laser beam that has a Gaussian beam profile. In this work we instead bleach a rectangular section of the fluid in a microchannel such that the problem reduces to a 1-D diffusion problem where the initial dye concentration after bleaching is an inverse top hat. The solution to the advection diffusion equation for an inverse top hat profile is given by Equation 32

$$C(x,t) = C_o - \frac{C_o}{2}\left[\operatorname{erf}\left(\frac{h-x}{\sqrt{4Dt}}\right) + \operatorname{erf}\left(\frac{h+x}{\sqrt{4Dt}}\right)\right] \tag{32}$$

where C is the concentration of the dye (or the molecule the dye is attached to), C_o is the initial concentration of the dye, h is the initial width of the bleach region, x is the spatial coordinate, D is the diffusivity of the dye and t is time. At each time the concentration profile at each time is fit to Equation 32 so that the diffusivity can be calculated. The mean diffusivity over the course of the recovery period is then used and the diffusivity coefficient of the dye.

In order to fit the measured intensity profiles to this form it is required to renormalize the profile after the flatfield and backfield correct so that the bleached region is initially at zero concentration and the unbleached areas have a concentration equal to the input concentration. This is necessary because usually the bleaching is not complete and there is some unintended bleaching of the whole field of view while imaging the recovery. Figure 17 shows an example of the recovery profiles over time and includes the fits of Equation 32. The width of the initially bleached region is calculated based on the region where the first post-bleach image reaches 50% of the original concentration.

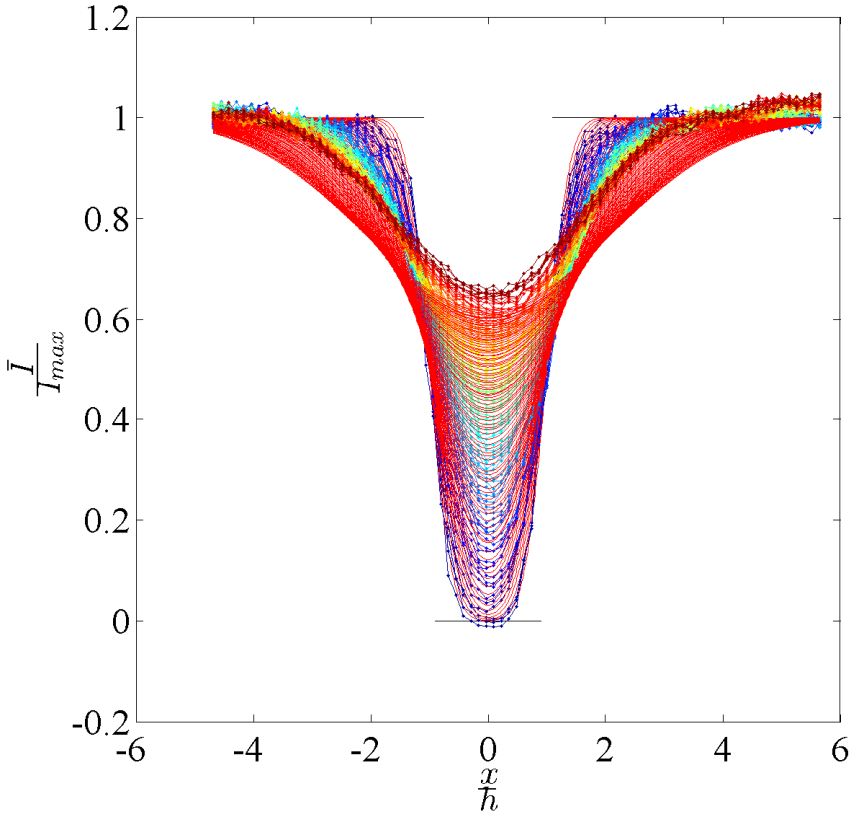

Figure 17. The concentration recovery of an inverse top hat profile after photobleaching. The experimentally measured concentrations (•) are plotted at each time along with the theoretical solutions from Equation 32 (solid lines).

3.3.7 FRAP experimental procedure.

The FRAP experiments are conducted on a Leica SP2 confocal system (Leica Microsystems, Buffalo Grove, IL) using a 20x objective and a 488nm Ar laser. The FRAP solutions are hand loaded into PDMS microchannels bonded to glass coverslips. The channels are 50 μm wide and 30 μm deep and several millimeters long. A region of interest that completely covered the width of the channel was bleached. This reduces the

diffusion to a 1-D problem where dye is in an inverse top-hat profile. Equation (31 is used to calculate the concentration inside the channel. The recovery of the bleached region is monitored for 90 frames at a frame rate of 0.513 Hz. The concentration profiles are fitted to the analytical solution of the advection-diffusion equation for an inverse top-hat profile to obtain a least-squares fit of the diffusivity at each time. The diffusivity is then temporally averaged to get diffusivity of the 2 MDa probe at each sugar concentration. The early time diffusivities are excluded in this average to account for uncertain in between the bleach time and the start of the recovery time. The measured diffusivity of the probe, D_{pr}, as a function of the sugar concentration is shown in Figure 18. The probe diffusivity is scaled by the diffusivity of the probe in water, D_o. The diffusivity of the probe in the sugar solution is given by Equation (33 (Phillies, Gong, Li, Ran, Zhang, Yu and Rolling, 1989)

$$\frac{D}{D_o} = \exp\left(-\beta C_s\right) \tag{33}$$

where β is a coefficient that depends the properties of the probe and the sugar and has units of mL/g of sugar. Equation (33 can also be derived from the Stokes-Einstein equation when the viscosity scales as $\exp(\beta C_s)$ (Philliges, 2011). It is important to measure the diffusivity of the probe in the sugar so that any sugar-probe interactions are captured in the measurement. Figure 18 shows the measured probe diffusivity versus sugar concentration from FRAP. For the probe and sugar combinations used in these experiments D_o=5.9 ($\mu m^2/s$) and β=29.09 (mL/g of sugar).

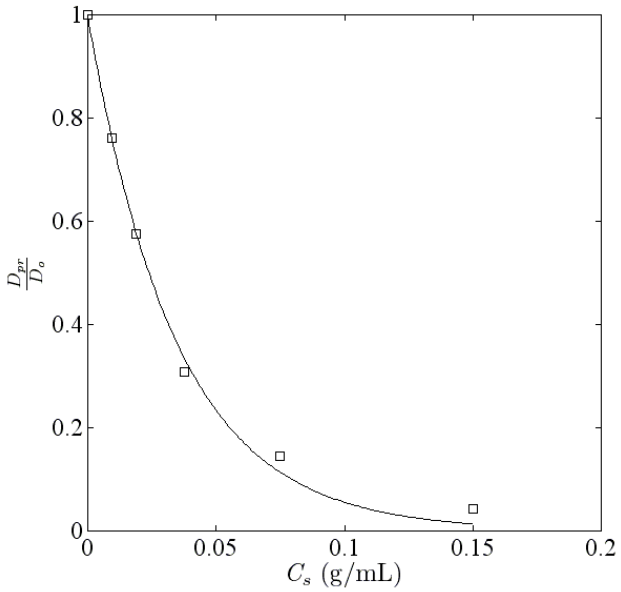

Figure 18. The diffusivity of the probe measured using FRAP scaled by the probe diffusivity in water vs. the concentration of sugar in (g/mL). The solid line is the fit data using Equation (33 which gives D_o=5.9 (μm2/s) and β=29.09 (mL/g of sugar).

3.4 Results and Discussion

Figure 19a shows the measured sugar concentration in the channel for three different experiments. We classify the experiments by the maximum measured sugar concentration, here C_{max} 0.006, 0.0275, and 0.031g/mL. This classification does not completely describe the results but it serves as a useful reference point to help order the outcomes of the experiments. We do not use input concentration of sugar into the top channel because the concentration in the bottom channel is not consistent between experiments or devices for a given input sugar concentration. The hindered transport of the sugar through the membrane results in only a fraction of the sugar diffusing through the membrane and can result in sugar building up near the outlet channel. Fick's first law suggests that the sugar concentration should be linear in the center channel and that the

strength of concentration gradient is proportional to the difference between the inlet and outlet sugar concentrations, the partitioning coefficient of the sugar through the membrane, and inversely proportional to the total distance between the inlet and outlet channels. The measured sugar concentrations in Figure 19a are roughly linear. The sugar gradients are lower than expected based on the difference in sugar inlet and outlet concentrations and the Equations 15 and 16 due to the low partitioning coefficient of the membranes. When imaging under and near the control channels the intensity of the sugar in the control channels affects the measurement of the sugar in the bottom channel and therefore the sugar concentration and diffusivity are cropped in these regions. Figure 19 shows the empirically calculated diffusivity of the probe molecules in the measured sugar concentrations from Figure 19a. The diffusivity is calculated by plugging the measured sugar concentration into Equation (33 with the coefficients determined from Figure 18. The diffusivity is approximately linear and is highest in the region of low sugar concentration and lowest in the region of high sugar concentration.

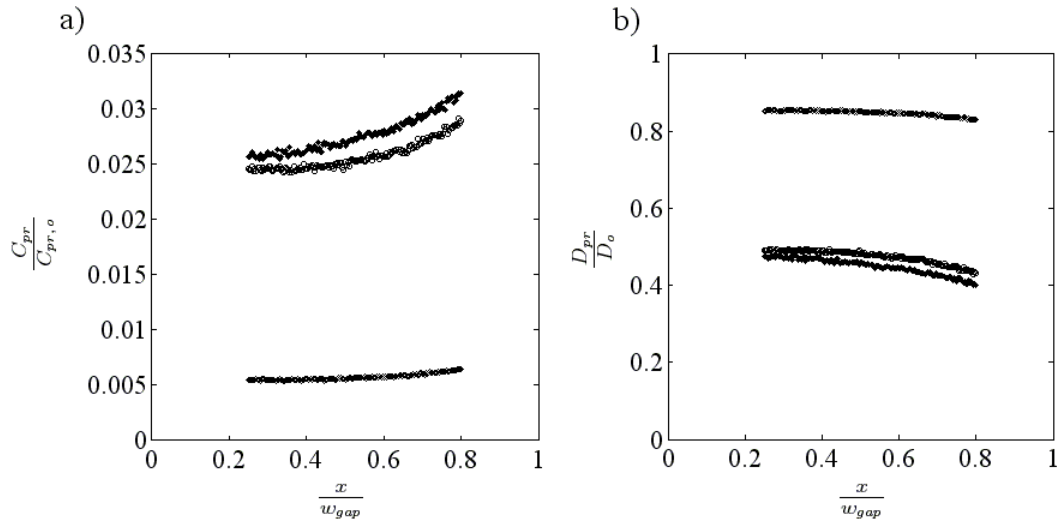

Figure 19. a) The steady state sugar concentrations vs. the scaled channel width for C_{max} 0.006 (Δ), 0.0275 (○), and 0.031g/mL (•). b) The steady state probe diffusivity scaled by the probe diffusivity in water vs. the scaled channel width for C_{max} 0.006 (Δ), 0.0275 (○), and 0.031g/mL (•).

Figure 20a shows the temporal response of probe concentration across the channel for a maximum measured sugar concentration of 0.031 g/mL. Figure 20a shows that the probe concentration reaches steady state in approximately 15min. This time is much greater than the setup time for the sugar concentration which is ~1.5 min. Figure 20b shows the steady state probe concentration, C_{pr}, scaled by the input probe concentration, $C_{pr,o}$, versus the scaled channel width for the same three sugar concentrations shown in Figure 19. The probe concentrations are shown for the full channel gap since the probe is confined to the bottom channel. The measured responses for each maximum sugar concentration are linear. The probes reach a pseudo equilibrium distribution where there is a higher concentration of probe molecules in the low diffusivity region at any given time than are in the high diffusivity region. The strength of the probe concentration scales

with the maximum measured sugar concentration. Each experimental condition is accompanied by a theoretical solution from Equation (25) with α=0, shown in Figure 20b by solid lines. The diffusivity profile used in the theoretical solution is determined from linear fits of the diffusivity from Figure 19b.

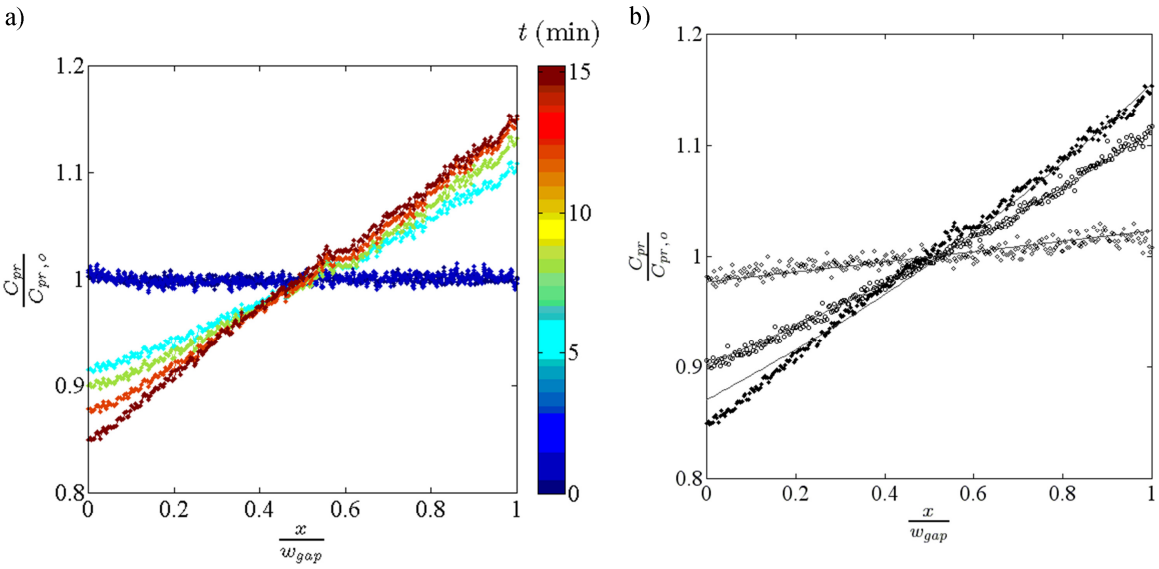

Figure 20. a) The temporal response of probe concentration across the channel for a maximum measured sugar concentration of 0.031 g/mL. b) The steady state probe concentrations scaled by the input probe concentration vs. the scaled channel width for C_{max} 0.006 (Δ), 0.0275 (○), and 0.031g/mL (•). The solid lines represent the theoretical probe concentration at steady state given the diffusivity gradients for each experiment in Figure 19b from the Fokker-Planck equation for variable diffusivity (Equation (25)).

The strength of the probe concentration in response to the diffusivity is governed by the steady state condition for the probe. At steady state the net flux of the probes in the channel has to be zero as described by Equation (24. A good reference point for this calculation is the center of the channel. In these experiments the probe concentration to the left is lower than the input concentration while everything to the right of this point is

higher. The no net flux condition is a balance of Fickian diffusion from right to left and diffusive flux (flux from gradients in diffusivity) from left to right. This balance is demonstrated in Figure 21 where the probe gradient is scaled by the probe input concentration and multiplied the channel gap is plotted versus the probe diffusivity gradient scaled by the mean diffusivity and multiplied by the channel gap. These terms represent the competing flux terms from Equation (24 after it has been rearranged and non-dimensionalized. Figure 21 shows the results from eight different experiments including the three shown in Figure 19 and Figure *20*. The solid line represents the analytical solution from Equation (24. For these experiments it was determined that α=0 which is consistent for the Ito convention for the Langevin equations for Brownian particles (Risken, 1989). The experimentally calculated net flux agrees well with the analytical solution. Figure 21 shows that the greater the magnitude of the gradient in diffusivity, the higher the gradient in probe concentration. Inversely the higher the mean diffusivity in the channel the lower probe concentration gradient. This highlights an important dichotomy of bounded variable diffusivity random walk. A gradient in diffusivity is a necessary but not a sufficient condition for achieving a gradient in concentration. As previously established (Grassia et al., 1995; Schitzner, 1993; Visser, 2008) in addition to a diffusivity gradient the diffusion characteristics of the probe have to be such that α is nonzero and the system needs to be bounded. There can also some situations where these conditions are meet but no gradient is observed. In order to get a measurable probe concentration gradient the mean probe diffusivity has to small compared to the diffusivity gradient. This is because the process relies on the dwell time

for the particles being higher in some areas than others. This makes sense from a pure diffusion standpoint because the higher the mean diffusivity the more quickly and concentration gradients are smoothed out.

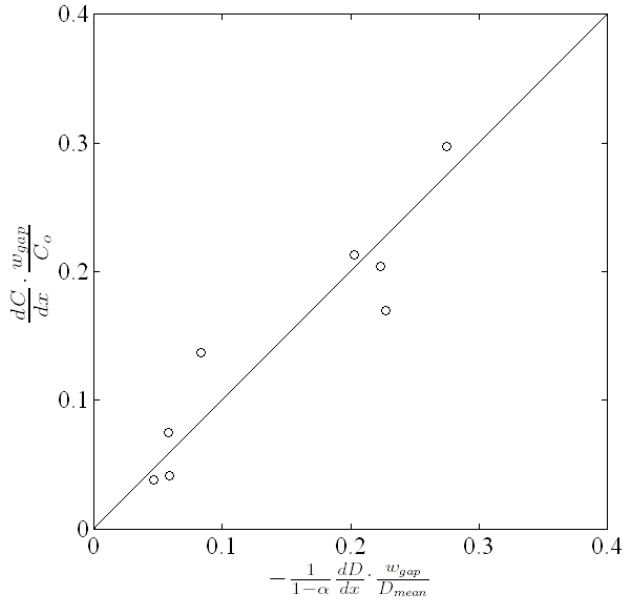

Figure 21. The steady state scaled probe concentration gradient vs. steady state scaled diffusivity gradient. The concentration gradient is scaled by the gap between the input and output channels over the minimum probe gradient in the channel. The diffusivity gradient is scaled by the gap between the input and output channels over the minimum probe diffusivity in the channel times 1-α. The theoretical solution from Equation (**24** is the solid line.

3.5 Conclusions

A variable diffusivity random walk system is created using a microfluidic gradient generating device. The diffusivity gradient is created by a viscosity gradient, which is generated through a concentration gradient of sugar (10 kDa dextran). The measured sugar concentration in the center channel is linear in accordance with expectations from Fick's laws. The diffusivity is empirically calculated using the

measured sugar concentration and the measure diffusivity of the probe from FRAP. Despite the fact that the diffusivity depends nonlinearly on the sugar concentration the diffusivity in the center channel is approximately linear because the sugar concentration gradient is weak. This is due to the low partitioning of the sugar through the device membranes. The diffusivity gradient leads to a concentration gradient of probe molecules (2 MDa dextran). At steady state the probes possess a slightly higher concentration in regions of low diffusivity. The strength of the probe concentration gradient is proportional to the strength of the diffusivity gradient and inversely proportional to the mean probe diffusivity in the channel in accordance with the no flux condition at steady state. The measured probe concentration gradient agrees with the Fokker-Planck equation for variable diffusivity when α=0. The applicability of the Fokker-Planck equation our system suggests that any particle or microorganism can be concentrated in a diffusivity gradient as long as the system is bounded, the mean diffusivity is small compared to the magnitude of the diffusivity gradient, and α is not equal to 1. This means that the motion of any object is capable of being passively controlled using a diffusivity gradient.

CHAPTER 4

SUMMARY

At low Reynolds number motile particles are classified by their effective diffusivity. Generic circle swimmer motors (not necessarily catalytic motors) exhibit short and long-time diffusivities that scale as $v^2/2\omega$ and $v^2/[2D_r(1+(\omega/D_r)^2)]$ respectively. These time scales arise due to the rotational velocity of the motors. When observed over short-times, or when the motors are confined to small spaces, the motors will appear to have a different diffusivity than at long-times or in large spaces. Artificial swimmers can exhibit maxima in long-time effective diffusivities if the motors have nonlinear translational or rotational velocities, or if the rotational diffusivity is a function the physical controlling parameter, in this work fuel concentration. This means that circle swimmers can exhibit chemokinesis in bounded fuel concentration gradients. The chemokinetic response of particles is a result of the response to a diffusivity gradient in a confined space. The Fokker-Planck equation for variable diffusivity describes the chemokinetic response in such a system. A variable diffusivity random walk system is created using a microfluidic gradient generating device. The diffusivity gradient is created by a viscosity gradient, which is generated through a concentration gradient of sugar (10 kDa dextran). The strength of the probe concentration gradient is proportional to the strength of the diffusivity gradient and inversely proportional to the mean probe diffusivity in the channel in accordance with the no flux condition at steady state. Our work suggests that any organism can be concentrated in a

diffusivity gradient as long as the system is bounded, the mean diffusivity is small compared to the magnitude of the diffusivity gradient, and α is not equal to 1.

REFERENCES

Abhyankar, V. V., Toepke, M. W., Cortesio, C., Lokuta, M. A., Huttenlocher, A., & Beebe, D. J. (2008). A platform for assessing chemotactic migration within a spatiotemporally defined 3D microenvironment. *Labon a Chip, 8*, 1507-1515. doi:10.1039/b803533d

Ahmed, T., Shimizu, T. S., & Stocker, R. (2010). Bacterial Chemotaxis in Linear and Nonlinear Steady Microfluidic Gradients. *Nano Letters, 10*, 3379-3385. doi:10.1021/nl101204e

Ahmed, T., Shimizu, T. S., & Stocker, R. (2010). Microfluidics for bacterial chemotaxis. *Integrative Biology, 2*, 604-629. doi:10.1039/c0ib00049c

Anderson, J. L. (1989). Colloid Transport by Interfacial Forces. *Annual Review of Fluid Mechanics, 21*, 61-99. doi:10.1146/annurev.fl.21.010189.000425

Aran, K., Sasso, L. A., Kamdar, N., & Zahn, J. D. (2010). Irreversible, direct bonding of nanoporous polymer membranes to PDMS or glass microdevices. *Lab Chip, 10*, 548-552. doi:10.1039/b924816a

Armstrong, J. K., Wenby, R. B., Meiseman, H. J., & Fisher, T. C. (2004). The hydrodynamic radii of marcromolecules and their effect on red blood cell aggregation. *Biophysical Journal, 87*, 4259-4270. doi:10.1529/biophysj.104.047746

Axelrod, D., Koppel, D. E., Schlessinger, J., Elson, E., & Webb, W. W. (1976). Mobility Measurement by Analysis of Fluorescence Photobleaching Recovery Kinetics. *Biophysical Journal, 16*, 1055-1069. doi:10.1016/S0006-3495(76)85755-4

Balasubramanian, S., Kagan, D., Manesh, K., Calvo-Marzal, P., Flechsig, U. W., & Wang, J. (2009). Thermal modulation of nanomotor movement. *Small, 5*, 1569-1574. doi:10.1002/smll.200900023

Berg, H. C. (1975). Chemotaxis in Bacteria. *Annual Review of Biophysics and Bioengineering, 4*, 119-136. doi:10.1146/annurev.bb.04.060175.001003

Berg, H. C., & Brown, D. A. (1972). Chemotaxis in Escherichia coli analysed by Three-dimensional Tracking. *Nature, 239*, 500-504. doi:10.1038/239500a0

Brunner, C., Wahnes, C., & Vogel, V. (2007). Cargo pick-up from engineered loading stations by kinesin driven molecular shuttles. *Lab Chip, 7*, 1263-1271. doi:10.1039/B707301A

Burdick, J., Laocharoensuk, R., Wheat, P. M., Posner, J. D., & Wang, J. (2008). Synthetic nanomotors in microchannel networks: Directional microchip motion and controlled manipulation of cargo. *Journal of the American Chemical Society, 130*, 8164–8165. doi:10.1021/ja803529u

Calvo-Marzal, P., Manesh, K. M., Kagan, D., Balasubramanian, S., Cardona, M., Flechsig, G. U., . . . Wang, J. (2009). Electrochemically-triggered motion of catalytic nanomotors. *Chemical Communications*, 4509–4511. doi:10.1039/B909227G

Chaturvedi, N., Hong, Y., Sen, A., & Velegol, D. (2010). Magnetic enhancement of phototaxing catalytic motors. *Langmuir, 26*, 1692–1712. doi:10.1021/la904133a

Cussler, E. L. (2009). *Diffusion: Mass Transfer in Fluid Systems.* Cambridge, UK: Cambridge University press.

Dhar, P., Fischer, T. M., Wang, Y., Mallouk, T. E., Paxton, W. F., & Sen, A. (2006). Autonomously moving nanorods at a viscous interface. *Nano Letters, 6*, 66–72. doi:10.1021/nl052027s

Doot, R. K., Hess, H., & Vogel, V. (2007). Engineered networks of oriented microtubule filaments for directed cargo transport. *Soft Matter, 3*, 349-356. doi:10.1039/B607281J

Duffy, D. C., McDonald, J. C., Schueller, O. J., & Whitesides, G. M. (1998). Rapid prototyping of microfluidic systems in poly(dimethylsiloxane). *Analytical Chemistry, 70*, 4974-4984. doi:10.1021/ac980656z

Ebbens, S. J., & Howse, J. R. (2010). In pursuit of propulsion at the nanoscale. *Soft Matter, 6*, 726–738. doi:10.1039/B918598D

Ebbens, S., Jones, R., Ryan, A., Golestanian, R., & Howse, J. R. (2010). Self-assembled autonomous runners and tumblers. *Physical Review E, 82*, 0153304(R). doi:10.1103/PhysRevE.82.015304

Engelmann, T. W. (1881). Neue methoden zur untersuchung der sauerstoffausscheidung pflanzlicher und tierischer organismen. *Pflüger's Archiv Gesamte Physiol, 39*, 285-92.

Fournier-Bidoz, S., Arsenault, A. C., Manners, I., & Ozin, G. A. (2005). Synthetic self-propelled nanorotors. *Chemical Communications*, 441-443. doi:10.1039/B414896G

Gibbs, J. G., & Zhao, Y. P. (2009). Design and characterization of rotational multicomponent catalytic nanomotors. *Small, 5*, 2304–2308. doi:10.1002/smll.200900686

Gibbs, J. G., Kothari, S., Saintillan, D., & Zhao, Y. P. (2011). Geometrically designing the kinematic behavior of catalytic nanomotors. *Nano Letters, 11*, 2543–2550. doi:10.1021/nl201273n

Goel, A., & Vogel, V. (2008). Harnessing biological motors to engineer systems for nanoscale transport and assembly. *Nature Nanotechnology, 3*, 465–475. doi:10.1038/nnano.2008.190

Grassia, P. S., Hinch, E. J., & Nitsche, L. C. (1995). Computer simulations of Brownian motion of complex systems. *Journal of Fluid Mechanics, 282*, 373-403. doi:10.1017/S0022112095000176

Happel, J., & Brenner, H. (1983). *Low Reynolds number hydrodynamics: With special applications to particulate media.* New York City: Springer-Verlag.

Hess, H. B. (2004). Powering nanodevices with biomolecular motors. *Chemistry-a European Journal, 10*, 2110–2116. doi:10.1002/chem.200305712

Hong, Y., Blackman, N. M., Kopp, N. D., Sen, A., & Velegol, D. (2007). Chemotaxis of nonbiological colloidal rods. *Physcial Review Letters, 99*, 178103. doi:10.1103/PhysRevLett.99.178103

Howse, J. R., Jones, R. A., Ryan, A. J., Gough, T., Vafabakhsh, R., & Golestanian, R. (2007). Self-Motile colloidal particles: From directed propulsion to random walk. *Physical Review Letters, 99*, 048102-48105. doi:10.1103/PhysRevLett.99.048102

Ibele, M., Mallouk, T. E., & Sen, A. (2009). Schooling behavior of light-powered autonomous micromotors in water. *Angewandte Chemie, 48*, 3308–3312. doi:10.1002/anie.200804704

Ismagilov, R. F., Schwartz, A., Bowden, N., & Whitesides, G. M. (2002). Autonomous movement and self-assembly. *Angewandte Chemie, 114*, 674–676. doi:10.1002/1521-3757(20020215)114:4<674::AID-ANGE674>3.0.CO;2-Z

Kagan, D., Calvo-Marzal, P., Balasubramanian, S., Sattayasamitsathit, S., Manesh, K. M., Flechsig, G. U., & Wang, J. (2009). Chemical sensing based on catalytic nanomotors: Motion-Based detection of trace silver. *Journal of the American Chemical Society, 131*, 12082–12083. doi:10.1021/ja905142q

Keller, H. U., Wilkinson, P. C., Abercrombie, M., Becker, E. L., Hirsch, J. G., Miller, M. E., . . . Zigmond, S. H. (1977). A proposal for the definition of terms related to locomotion of leukocytes and other cells. *CELL BIOLOGY INTERNATIONAL REPORTS, 1*, 391-397. doi:10.1016/0309-1651(77)90072-8

Kline, T. R., Iwata, J., Lammert, P. E., Mallouk, T. E., Sen, A., & Velegol, D. (2006). Catalytically driven colloidal patterning and transport. *Journal of Physical Chemistry B, 110*, 24513–24521. doi:10.1021/jp0643931

Laocharoensuk, R., Burdick, J., & Wang, J. (2008). Carbon-Nanotube-Induced acceleration of catalytic nanomotors. *ACS Nano, 2*, 1069–1075. doi:10.1021/nn800154g

Long, T., & Ford, R. M. (2009). Enhanced Transverse Migration of Bacteria by Chemotaxis in a Porous T-Sensor. *Environmental Science & Technology, 43*, 1546-1552. doi:10.1021/es802558j

Manesh, K. M., Cardona, M., Yuan, R., Clark, M., Kagan, D., Balasubramanian, S., & Wang, J. (2010). Template-Assisted fabrication of salt-independent catalytic tubular microengines. *ACS Nano, 4*, 1799–1804. doi:10.1021/nn1000468

Marine, N. A., & Posner, J. D. (2013). Chemokinesis of Non-Swimmers. *PRL*.

Marine, N. A., Wheat, P. M., Ault, J., & Posner, J. D. (2013). Diffusive behaviors of circle-swimming motors. *Physical Review E, 87*, 052305. doi:10.1103/PhysRevE.87.052305

Mirkovic, T., Zacharia, N. S., Scholes, G. D., & Ozin, G. A. (2009). Nanolocomotion—Catalytic nanomotors and nanorotors. *Small, 6*, 159–167. doi:10.1002/smll.200901340

Moran, J. L., & Posner, J. D. (2011). Electrokinetic locomotion due to reaction-induced charge auto-electrophoresis. *Journal of Fluid Mechanics, 680*, 31-66. doi:doi:10.1017/jfm.2011.132

Moran, J. L., Wheat, P. M., & Posner, J. D. (2010). Locomotion of electrocatalytic nanomotors due to reaction induced charge autoelectrophoresis. *Physical Review E, 81*, 065302(R). doi:10.1103/PhysRevE.81.065302

Paxton, W. F., Baker, P. T., Kline, T. R., Wang, Y., Mallouk, T. E., & Sen, A. (2006). Catalytically induced electrokinetics for motors and micropumps. *Journal of the American Chemical Society, 128*, 14881–14888. doi:10.1021/ja0643164

Paxton, W. F., Kistler, K. C., Olmeda, C. C., Sen, A., St. Angelo, S. K., Cao, Y., . . . Crespi, V. H. (2004). Catalytic nanomotors: Autonomous movement of striped nanorods. *Journal of the American Chemical Society, 126*, 13424–13431. doi:10.1021/ja047697z

Paxton, W. F., Sen, A., & Mallouk, T. E. (2005). Motility of catalytic nanoparticles through self-generated forces. *Chemistry a European Journal, 11*, 6462–6470. doi:10.1002/chem.200500167

Philliges, G. D. (2011). *Phenomenology of Polymer Solution Dynamics.* Cambridge, UK: Cambridge University Press.

Purcell, E. M. (1977). Life at Low Reynolds Number. *American Journal of Physics, 45*, 3-11. doi:10.1119/1.10903

Risken, H. (1989). *The Fokker-Planck Equation.* Berlin, Germany: Springer-Verlag.

Sabass, B., & Seifert, U. (2012). Nonlinear, electrocatalytic swimming in the presence of salt. *Journal of Chemical Physics, 136*, 214507. doi:10.1063/1.4719538

Schnitzer, M. J. (1993). Theory of continuum random walks and application to chemotaxis. *Physical Review E, 48*, 2553-2568. doi:10.1103/PhysRevE.48.2553

Squires, T. M. (2010). Cross-stream migration vs. differential relaxation: Non-Boltzmann distribution of polymers and particles in dissipative systems. *ArXiv*, 1-10.

Staffeld, P. O., & Quinn, J. A. (1988). Diffusion-Induced banding of colloid particles via diffusiophoresis. *Journal of Colloid and Interface Science, 130*, 88-100. doi:10.1016/0021-9797(89)90080-5

Sundararajan, S., Lammert, P. E., Zudans, A. W., Crespi, V. H., & Sen, A. (2008). Catalytic motors for transport of colloidal cargo. *Nano Letters, 8*, 1271–1276. doi:10.1021/nl072275j

Takagi, D., Braunschweig, A., Zhang, J., & Shelley, M. J. (2013). Dispersion of self-propelled rods undergoing fluctuation-driven flips. *Physical Review Letters, 110*, 038301. doi:10.1103/PhysRevLett.110.038301

van den Heuvel, M. G., & Dekker, C. (2007). Motor proteins at work for nanotechnology. *Science, 317*, 333–336. doi:10.1126/science.1139570

van Teeffelen, S., & Lowen, H. (2008). Dynamics of a Brownian circle swimmer. *Physical Review E, 78*, 020101(R). doi:10.1103/PhysRevE.78.020101

van Teeffelen, S., Zimmermann, U., & Lowen, H. (2009). Clockwise-directional circle swimmer moves counter-clockwise in Petri dish- and ring-like confinements. *Soft Matter, 5*, 4510-4519. doi:10.1039/B911365G

Visser, A. W. (2008). Lagrangian modelling of plankton motion: From deceptively simple random walks to Fokker–Planck and back again. *Journal of Marine Systems, 70*, 287–299. doi:10.1016/j.jmarsys.2006.07.007

Wang, J. (2009). Can man-made nanomachines compete with nature biomotors? *ACS Nano, 3*, 4–9. doi:10.1021/nn800829k

Wang, Y., Hernandez, R. M., Bartlett Jr, D. J., Bingham, J. M., Kline, T. R., Sen, A., & Mallouk, T. E. (2006). Bipolar electrochemical mechanism for the propulsion of catalytic nanomotors in hydrogen peroxide solutions. *Langmuir, 22*, 10451–10456. doi:10.1021/la0615950

Wheat, P. M., Marine, N. A., & Posner, J. D. (2013). Collective Behavior of Swimming Bimetallic Motors. *Arxiv*.

Wheat, P. M., Marine, N. A., Moran, J. L., & Posner, J. D. (2010). Rapid Fabrication of Bimetallic Spherical Motors. *Langmuir, 26*, 13052–13055. doi:10.1021/la102218w

Zigmond, S. H., & Hirsch, J. G. (1973). Leukocyte locomotion and chemotaxis: New for evaluation and demonstration of a cell-derived chemotactic factor. *The Journal of Experimental Medicine, 137*, 387-410 . doi:10.1084/jem.137.2.387

APPENDIX A

BROWNIAN DYNAMICS SIMULATIONS

```
%simulate behavior brownian particles in a 1-D diffusivity gradient due to viscosity
cont =1; %are we working from previous data 0 for no, 1 for yes
if cont == 0
   clc, clear all,close all
   cont=0;
else
   close all
end

dt=.1;%s timestep period
numframes=2600;numrods=10000;
t(:,1)=0:dt:(numframes-1)*dt;

theta=zeros(numframes,numrods);%x=zeros(numframes,numrods);%y=zeros(numframes
,numrods);

%particle setup - constants
d=.5;%particle diameter in um
a=d/2;
%constants for Brownian Do for water
k=1.38e-23;T=(23+273);mu=1e-3;%m^2*kg/(s^2*K), K, kg/m/s
Do=k*T/(6*pi*mu*a*10^-6);
%vscale library - 1D
%vscale=1.70;wscale=2.50*pi/8;%3um spheres Deff 0.145um^2/s
```

```
% vscale=6.00;wscale=2.50*pi/8;%250nm spheres Deff 1.77um^2/s - wscale not set

% vscale=2.93;wscale=2.50*pi/8;%1um spheres Deff 0.43873um^2/s - wscale not set

vscale=4.2;wscale=2.50*pi/8;%500nm spheres Deff 0.86741um^2/s - wscale not set

% vscale=6.00;wscale=2.50*pi/8;%vscale and wscale set to level to achieve brownian values of Deff~.144,Drot~.0447 for dt=0.1

%choose channel geometry (ch=1 (triangular), ch=2 thinning

ch=3;

if ch==1

   %linear visc gradient with mu_o on left and mu_w on right

   w = 300;%width of channel in um

   mu_o=1000e-3;%oil - dynamic visc in kg/(m*s)

   mu_w=1e-3;%water - dynamic visc in kg/(m*s)

   xL=0;xR=w;

   if cont ==0

      x(1,:)=linspace(xL,xR,numrods);%evenly distribute the motors

   end

elseif ch==2

   %non-linear visc gradient with mu_o on left and mu_w on right

   w = 300;%width of channel in um

   mu_o=50e-3;%dextran - dynamic visc in kg/(m*s)

%     cpR=.2;%the concentration in w/v% at the right boundary that gives mu_o

%     mu_w=1e-3;%water - dynamic visc in kg/(m*s)

%     C2=15.3;%fit non-linear so excel file dextran gives this fit

   %new conditions that reflect SS soln to flux balance
```

```
    C2=.143;%the concentration in w/v% at the right boundary that gives mu_o
    C3=.057;
    mu_w=1e-3;%water - dynamic visc in kg/(m*s)
    alpha=10.73;%fit non-linear so excel file dextran gives this fit
    xL=0;xR=w;
    if cont ==0
       x(1,:)=linspace(xL,xR,numrods);%evenly distribute the motors
    end
elseif ch==3
    %double layer non-linear visc gradient with mu_o on left and mu_w on right
    w = 300;%distance in between edges of input channels in um
    w_cL=50;%width of the high visc input channel in um
    w_cR=50;%width of the low visc input channel in um
    w_L=0;%length of excess channel to left(near high visc channel)
    w_R=0;%length of excess channel to right (after low visc channel)
    C2=.27;%the concentration in w/v% at the right boundary that gives mu_o
    C3=.02;%concentrations determined by membrane thickness of ~15um
%     C2=.5;%the concentration in w/v% at the right boundary that gives mu_o
%     C3=0;%concentrations determined by membrane thickness of ~100um
    mu_w=1e-3;%water - dynamic visc in kg/(m*s)
    alpha=10.73;%fit non-linear so excel file dextran gives this fit
    xL=0;xR=w_L+w_cL+w+w_cR+w_R;%beginning and end of beginning observation
channel
    if cont ==0
```

```
        x(1,:)=linspace(xL,xR,numrods);%evenly distribute the motors
    end
end


if cont == 0
    count=1;
    for i =2:numframes
        rx=vscale*randn(1,numrods);
%         rw=wscale*randn(1,numrods);
%         theta(i,:)= theta(i-1,:)+rw*dt;
        F_h_x=zeros(1,numrods);
        if ch==1
            F_h_x(1,:)=(1-mu_w/mu_o)*x(i-1,:)/w + mu_w/mu_o;%assume linear gradient
        elseif ch==2
            F_h_x(1,:)=mu_w./(mu_w*exp(alpha*(C2-(C2-C3)*x(i-1,:)/w)));%assume
nonlinear gradient
        elseif ch==3


            %in w_L or under w_cL (C=C2)
            ind=find(x(i-1,:)<w_L+w_cL);
            F_h_x(1,ind)=mu_w./(mu_w*exp(alpha*C2*ones(1,length(ind))));%assume
uniform concentration
            %in between channels linear C2 to C3
            ind=find(x(i-1,:)>=w_L+w_cL & x(i-1,:)<=w_L+w_cL+w);
```

```
        F_h_x(1,ind)=mu_w./(mu_w*exp(alpha*(C2-(C2-C3)*(x(i-1,ind)-w_L-
w_cL)/w)));%assume nonlinear gradient

        %under w_cR or in w_R (C=C3)

        ind=find(x(i-1,:)>w_L+w_cL+w);

        F_h_x(1,ind)=mu_w./(mu_w*exp(alpha*C3(ones(1,length(ind)))));%assume
uniform concentration

    end

%           F_h_x=1;%this is for when we want to have normal diffusivity

%           x(i,:)= x(i-1,:)+F_h_x.*rx*dt;

    if ch ==1 || ch==2 || ch ==3 || ch==5

        x(i,:)= x(i-1,:)+F_h_x.*rx*dt;

        %test to see if any particles went out of bounds

        ind_R_ob=find(x(i,:)>xR);%test right wall

        if isempty(ind_R_ob) %if it's empty do nothing

        else,x(i,ind_R_ob)=xR-(x(i,ind_R_ob)-xR);%reflect particle about wall

%                                                   x(i,ind_R_ob)=x(i-1,ind_R_ob)-
F_h_x(ind_R_ob).*rx(ind_R_ob)*dt;%reflect particle about wall

        end

        ind_L_ob=find(x(i,:)<xL);%test left wall

        if isempty(ind_L_ob) %if it's empty do nothing

        else,x(i,ind_L_ob)=xL+(xL-x(i,ind_L_ob));%reflect particle about wall

%                                                   x(i,ind_L_ob)=x(i-1,ind_L_ob)-
F_h_x(ind_L_ob).*rx(ind_L_ob)*dt;%reflect particle about wall

        end

    end
```

```
        [n,xout] = hist(x(i,:),50);
        N(count,1:length(n))=n;count=count+1;Xout(count,1:length(n))=xout;
    end
else


end
%%%%%%%%%
%to be able to do longer times
for jj = 1:10
    x_store=x(numframes,:);theta_store=theta(numframes,:);
    theta=zeros(numframes,numrods);x=zeros(numframes,numrods);
    x(1,:)=x_store;theta(1,:)=theta_store;
    for i =2:numframes
        rx=vscale*randn(1,numrods);
%         rw=wscale*randn(1,numrods);
%         theta(i,:)= theta(i-1,:)+rw*dt;
        F_h_x=zeros(1,numrods);
        if ch==1
            F_h_x(1,:)=(1-mu_w/mu_o)*x(i-1,:)/w + mu_w/mu_o;%assume linear gradient
        elseif ch==2
            F_h_x(1,:)=mu_w./(mu_w*exp(alpha*(C2-(C2-C3)*x(i-1,:)/w)));%assume
nonlinear gradient
        elseif ch==3
            %in w_L or under w_cL (C=C2)
```

```
        ind=find(x(i-1,:)<w_L+w_cL);

        F_h_x(1,ind)=mu_w./(mu_w*exp(alpha*C2*ones(1,length(ind))));%assume
uniform concentration

        %in between channels linear C2 to C3

        ind=find(x(i-1,:)>=w_L+w_cL & x(i-1,:)<=w_L+w_cL+w);

        F_h_x(1,ind)=mu_w./(mu_w*exp(alpha*(C2-(C2-C3)*(x(i-1,ind)-w_L-
w_cL)/w)));%assume nonlinear gradient

        %under w_cR or in w_R (C=C3)

        ind=find(x(i-1,:)>w_L+w_cL+w);

        F_h_x(1,ind)=mu_w./(mu_w*exp(alpha*C3(ones(1,length(ind)))));%assume
uniform concentration

    end

    %    F_h_x=1;%this is for when we want to have normal diffusivity

    %    x(i,:)= x(i-1,:)+F_h_x.*rx*dt;

    if ch ==1 || ch==2 || ch ==3 || ch==5

        x(i,:)= x(i-1,:)+F_h_x.*rx*dt;

        %test to see if any particles went out of bounds

        ind_R_ob=find(x(i,:)>xR);%test right wall

        if isempty(ind_R_ob) %if it's empty do nothing

        else,x(i,ind_R_ob)=xR-(x(i,ind_R_ob)-xR);%reflect particle about wall

%                                                   x(i,ind_R_ob)=x(i-1,ind_R_ob)-
F_h_x(ind_R_ob).*rx(ind_R_ob)*dt;%reflect particle about wall

        end

        ind_L_ob=find(x(i,:)<xL);%test right wall

        if isempty(ind_L_ob) %if it's empty do nothing
```

```
        else,x(i,ind_L_ob)=xL+(xL-x(i,ind_L_ob));%reflect particle about wall
%                                                   x(i,ind_L_ob)=x(i-1,ind_L_ob)-
F_h_x(ind_L_ob).*rx(ind_L_ob)*dt;%reflect particle about wall
        end
      end
      [n,xout] = hist(x(i,:),50);
      N(count,1:length(n))=n;count=count+1;Xout(count,1:length(n))=xout;
   end
end
%%%%%%%%%
figure,plot(t,x(:,1),'k.'),%xlim([0 300]),ylim([0 300])
% figure,plot(t,x2(:,1),'k.'),
% figure,hist(x(numframes,:),50)%look at final distribution
% plotlabel('x (\mum)','N','Arial',24,0)
[a b]=hist(x(2600,:),30);
figure,bar(b,a/numrods,'k'),plotlabel('x  (\mum)','N','Arial',24,0),ylim([0  .4]),ylabel('$\bar
N$','interpreter','LaTex')
% figure,plot((1:count-1)*dt,N(:,1)/numrods),plotlabel('t(s)','N','Arial',24,0)
Nshift=N-circshift(N,[1,0]);
Nbar(2:length(N),1)=mean(abs(Nshift(2:length(N),:)),2);
figure,plot((2:count-1)*dt,Nbar(2:length(N),1)),plotlabel('t(s)','Nbar','Arial',24,0)
figure,hist(x(numframes,:)-x(1,:),100),plotlabel('\Deltax (\mum)','N_p','Arial',24,0)
```